

# 1 **Rock slope temperature evolution and micrometer-scale de-** 2 **formation at a retreating glacier margin**

3 Marc Hugentobler, Jordan Aaron, Simon Loew

4 Department of Earth Sciences, Engineering Geology, ETH Zurich, 8092 Zurich, Switzerland.

5 Corresponding author: Marc Hugentobler ([marc.hugentobler@erdw.ethz.ch](mailto:marc.hugentobler@erdw.ethz.ch))

6 Key points

- 7 • We monitor and model the subsurface temperature evolution and deformation in a rock slope during  
8 deglaciation.
- 9 • We observe a conduction dominated transient subsurface temperature regime adjusting to a new  
10 surface temperature following ice retreat.
- 11 • We document reversible deformation and irreversible rock mass damage and identify important  
12 drivers causing these deformations.

13 Abstract

14 In deglaciating environments, rock mass weakening and potential formation of rock slope instabilities is  
15 driven by long-term and seasonal changes in thermal- and hydraulic boundary conditions, combined with  
16 unloading due to ice melting. However, in-situ observations are rare. In this study, we present new monitor-  
17 ing data from three highly instrumented boreholes, and numerical simulations to investigate rock slope tem-  
18 perature evolution and micrometer-scale deformation during deglaciation. Our results show that the subsur-  
19 face temperatures are adjusting to a new, warmer surface temperature following ice retreat. Heat conduction  
20 is identified as the dominant heat transfer process at sites with intact rock. Observed nonconductive pro-  
21 cesses are related to groundwater exchange with cold subglacial water, snowmelt infiltration, or creek water  
22 infiltration. Our strain data shows that annual surface temperature cycles cause thermoelastic deformation  
23 that dominate the strain signals in the shallow thermally active layer at our stable rock slope locations. At  
24 deeper sensors, reversible strain signals correlating with pore pressure fluctuations dominate. Irreversible  
25 deformation, which we relate with progressive rock mass damage, occurs as short-term (hours to weeks)  
26 strain events and as slower, continuous strain trends. The majority of the short-term irreversible strain events  
27 coincides with precipitation events or pore pressure changes. Longer-term trends in the strain time series  
28 and a minority of short-term strain events cannot directly be related to any of the investigated drivers. We  
29 propose that the observed increased damage accumulation close to the glacier margin can significantly  
30 contribute to the long-term formation of paraglacial rock slope instabilities during multiple glacial cycles.

31 Plane language summary

32 Glaciers impose mechanical loads on the bedrock below and influence temperature and groundwater con-  
33 ditions in adjacent valley flanks. When glaciers retreat, the boundary conditions change, and related stress  
34 changes can weaken the adjacent rock mass. These processes potentially contribute to the long-term for-  
35 mation of rock slope instabilities. In this study, we investigate such processes based on rare borehole mon-  
36 itoring data with a focus on the subsurface temperature evolution and related deformations. Collected sub-  
37 surface rock temperatures reveal a warming trend following ice retreat that is strongly controlled by heat  
38 conduction. Observed non-conductive processes are related to groundwater exchange with cold subglacial  
39 water, snowmelt infiltration, or creek water infiltration. Our deformation data shows that thermomechanical

40 deformations related to annual surface temperature cycles are significant in the shallow 10 to 15 m. At  
41 greater depth, deformations related to changes in groundwater pressure dominate. Progressive rock mass  
42 damage, which is identified as the irreversible portion of the monitored deformation, occurs as fast and  
43 slow/continuous deformation. Precipitation events and groundwater pressure changes have been identified  
44 as important drivers for fast damage events. Drivers for continuous irreversible deformation remain uncer-  
45 tain but fatigue processes and presumably changing glacial loads are considered as potential causes.

46 Keywords

47 Subsurface temperature evolution; progressive rock mass damage; paraglacial rock slope evolution, bore-  
48 hole monitoring; rock slope deformation

## 49 1. Introduction

50 Rock slope failures are a major hazard in Alpine regions. The formation of rock slope instabilities is a long-  
51 term process related to progressive internal rock mass damage driven by various drivers that change over  
52 time (e.g., Gischig et al., 2016). There is a wide consensus that rock slopes experience a phase of increased  
53 stress perturbations during deglaciation, which potentially promotes the formation of rock slope instabilities  
54 (Ballantyne et al., 2014; Grämiger et al., 2020; McColl, 2012; McColl and Draebing, 2019; Prager et al.,  
55 2008; Riva et al., 2017). The most frequently discussed stress perturbations during deglaciation are related  
56 to mechanical unload due to glacial downwasting and perturbations in thermal and hydraulic boundary con-  
57 ditions (McColl and Draebing, 2019). The present work is focused on field investigations of the transient  
58 thermal regime induced by glacier retreat in adjacent valley slopes, and the related subsurface deformations.

59 As glaciers retreat, the stable thermal boundary conditions below glaciers are perturbed, which results in a  
60 “thermal shock” and long term cyclic thermal loading, that can induce long term rock mass damage  
61 (Grämiger et al., 2018). Until now, investigations on this topic were mainly based on numerical models and  
62 relied on assumptions unconstrained by in-situ data. The data presented herein is key to the understanding  
63 of heat transfer mechanisms in the subsurface, the timescales over which valley flanks adjust to the new  
64 thermal boundary conditions following deglaciation, as well as the magnitudes of thermomechanical  
65 stresses, which can lead to long term rock mass damage. Investigating these phenomena requires high  
66 resolution measurements of subsurface temperatures and deformation, which have never been recorded in  
67 alpine regions that feature temperate valley glaciers. Additionally, thermomechanical deformation signals  
68 can be overprinted e.g. by hydromechanical deformation (cf. Grämiger et al., 2020), and disentangling the  
69 two requires an understanding of slope hydrology, as well as measurements of pore pressure and precipi-  
70 tation events. Detailed investigations of hydraulic processes and hydromechanical deformations in our test  
71 site are presented in a companion publication.

72 Previous studies have used borehole temperature recordings to analyze the subsurface temperature regime  
73 and reconstruct past climate conditions (Bodri and Čermák, 1995; Bodri and Čermák, 1999; Pollack, 1993;  
74 Pollack et al., 1998; Pollack and Huang, 2000), as well as study permafrost processes (e.g., Gruber et al.,  
75 2004; Haberkorn et al., 2015; Schneider et al., 2012) and drivers of active rock slope instabilities (e.g.,

76 Gischig et al., 2011a; b; Moore et al., 2011). However, to the authors knowledge, subsurface temperature  
77 investigations in alpine environments undergoing glacial retreat below permafrost elevations have not been  
78 monitored in the past.

79 When considering the thermal regime of a rock slope, the glacier – rock slope interaction is controlled by  
80 both thermal and hydraulic conditions at the ice-rock interface. Bedrock in contact with temperate ice stays  
81 at the pressure melting point of the ice, which is around 0° C (Wegmann et al., 1998). When ice retreats,  
82 the previously covered bedrock surface is newly exposed to ambient temperature variations and solar radi-  
83 ation. These warmer temperatures then propagate to depth through a combination of conduction and ad-  
84 vection.

85 A conduction dominated subsurface temperature regime, which is expected in intact crystalline bedrock, is  
86 controlled by: 1) the surface temperature, which is subject to variability at daily to millennial timescales, 2)  
87 an outward flow of heat from the earth's interior, which can be considered constant at the relevant time-  
88 scales, 3) the thermal diffusivity of the medium, 4) latent heat effects from melting ice or freezing water in  
89 pores/cracks, and 5) the topography (Guéguen and Palciauskas, 1994; Pollack et al., 1998). In the case of  
90 homogenous subsurface thermal properties and flat topography, a steady-state temperature profile shows  
91 a constant rate of temperature increase with depth (dependent on the thermal conductivity and the heat flow  
92 from below). Surface temperature fluctuations then propagate as thermal waves at a pace governed by the  
93 thermal diffusivity, with amplitudes diminishing exponentially with depth (Pollack and Huang, 2000).

94 In reality, rock masses contain discontinuities, where fracture characteristics such as density, aperture, per-  
95 sistence, and connectivity control nonconductive heat transfer processes (e.g. advection of air or water),  
96 and heterogeneities (e.g. in the lateral thermal conductivity) potentially disturb the idealized heat conduction  
97 dominated subsurface temperature regime (Ge, 1998; Moore et al., 2011; Rybach and Pfister, 1994;  
98 Wegmann and Gudmundsson, 1999; Welch and Allen, 2014). Of particular importance to the present work  
99 are advective heat transfer processes driven by seasonal changes in rock slope hydrology in a glaciated  
100 valley, which influence the thermal regime. Transient pore pressures in such rock slopes are controlled by  
101 direct recharge to the fractured bedrock slope from snow melt in late spring and rainstorms in summer and  
102 fall, as well as by the englacial water pressure variations. Temperate glaciers carry large amounts of liquid

103 water, and a thin water film with pressures dependent on the glacial hydrological system is assumed to be  
104 present at greater depth at the glacier – rock interface (Lappegard et al., 2006).

105 Different types of temperature-coupled processes such as frost weathering, freeze-thaw cycles, and perma-  
106 frost degradation contribute to progressive rock mass weakening in alpine regions (Deprez et al., 2020;  
107 Draebing and Krautblatter, 2019; Draebing et al., 2017; Hales and Roering, 2007). Additionally, thermome-  
108 chanical stresses themselves can drive deformation and progressive rock mass damage in rock slopes  
109 (Gischig et al., 2011a; b; Marmoni et al., 2020; Mufundirwa et al., 2011). In the context of post- and late-  
110 glacial ice retreat, numerical investigations suggest that thermomechanical effects induced by long-term  
111 temperature variations related to glacial cycles and seasonal temperature variations induce significant ther-  
112 momechanical stresses to the valley flanks which can promote progressive rock mass damage (Baroni et  
113 al., 2014; Grämiger et al., 2018). These studies have shown that, during a glacial cycle, thermomechanically  
114 driven deformation and rock mass damage can be substantially higher than purely mechanical loading and  
115 unloading effects from glacier retreat or advance, and that the degree of fracturing (and the criticality of the  
116 fracture system in terms of its Mohr-Coulomb strength) is a an important factor controlling the amount of  
117 induced thermomechanical damage (Grämiger et al., 2018).

118 The aforementioned studies (Gischig et al., 2011a; b; Marmoni et al., 2020; Mufundirwa et al., 2011) have  
119 shown that thermomechanical stress perturbations (or stress perturbation of any origin) can drive reversible  
120 (elastic) deformation and irreversible (plastic) deformation related to progressive damage e.g., in the form  
121 of fracture propagation. The deformation characteristics strongly depend on the magnitude of the stress  
122 perturbation, as well as the rock mass properties and spatially varying in-situ stress levels that control the  
123 criticality of fractures in the system (Gischig et al., 2011a; b; Stock et al., 2012; Styles et al., 2011). If a  
124 stress perturbation occurs at a level below the critical stress threshold, it either mainly causes elastic (re-  
125 versible) deformation or if it exceeds a so-called fatigue limit it can lead to slow subcritical fatigue crack  
126 growth and hence minor plastic deformation (Attewell and Farmer, 1973; Brain et al., 2014). Processes  
127 contributing to subcritical crack growth can be both of cyclic nature (cyclic fatigue) or static (stress corrosion)  
128 (Cerfontaine and Collin, 2018; Eppes and Keanini, 2017). This has been observed in laboratory experiments  
129 and is described by several authors (e.g., Attewell and Farmer, 1973; Brown and Hudson, 1973; Cerfontaine

130 and Collin, 2018). Thus, such low stresses can also increase the criticality of a fracture to a level exceeding  
131 the fracture toughness, which enables the fracture to fail at an apparently random, low magnitude stress  
132 perturbation, complicating correlations with environmental drivers (Eppes and Keanini, 2017). In contrast,  
133 stress perturbations that occur at levels exceeding critical stress thresholds naturally can trigger instanta-  
134 neous plastic (irreversible) deformation.

135 In this study we use novel borehole monitoring data and numerical simulations to investigate the transient  
136 subsurface temperature regime and related micrometer-scale deformation in a rock slope adjacent to a  
137 temperate valley glacier undergoing rapid downwasting. We first analyze the borehole temperature and  
138 strain data and perform a statistical analysis of the strain data to highlight correlations between potential  
139 drivers and deformation events. We then use the borehole temperature data to estimate the depth-depend-  
140 ent apparent thermal diffusivity at our borehole locations, which is used to parameterize continuum 2D finite  
141 element models for heat conduction in the subsurface. Comparing these modeling results with temperature  
142 monitoring data provides insights into the transient subsurface temperature regime that follows glacier re-  
143 treat, as well as the dominant mechanisms governing heat transfer at our study site (conduction vs. advec-  
144 tion). Finally, we expand our finite element models to compute the expected thermoelastic deformation  
145 resulting from annual temperature cycles. These analyses provide crucial information regarding the relative  
146 importance of thermomechanical deformation on the total strain recorded at our instrumented rock slope,  
147 and hence its relevance for the overall observed deformation and progressive rock mass damage.

## 148 2. Site description

### 149 2.1. Geology and geomorphology

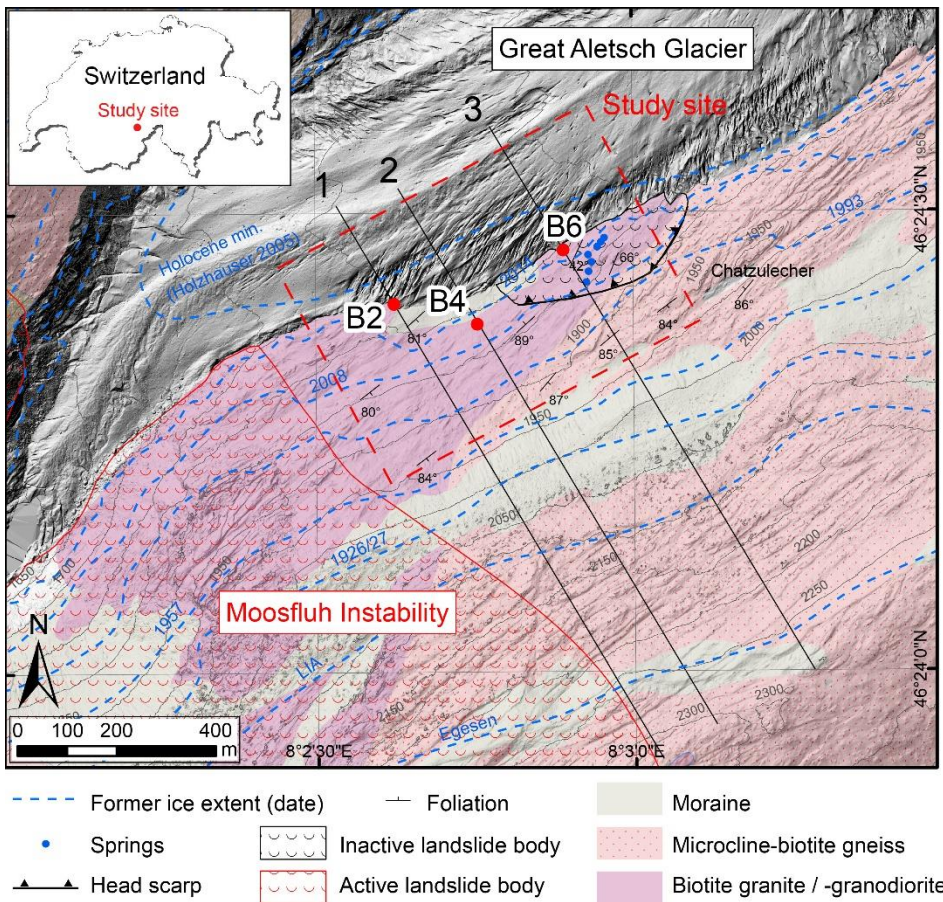
150 Our study site is located on the southern valley slope adjacent to the retreating glacier tongue of the Great  
151 Aletsch Glacier (Canton Valais, Switzerland) (see Fig. 1). The bedrock consists of fractured crystalline rocks  
152 (mainly gneisses and granites with thin schist layers) of the Aare-Massif (Steck, 2011). The rock slope is  
153 dipping NNW with an average slope angle of about 30° and the morphology is characterized by glacially  
154 smoothed bedrock surfaces with ridges and furrows. Furrows often follow weak schist layers or brittle-ductile  
155 shear zones normally oriented subparallel to the alpine foliation. This foliation strikes valley subparallel with  
156 a subvertical dip angle normally dipping into the slope. The rock mass is intersected by three persistent joint

157 sets with a normal spacing around 1 to 3 m at the ground surface (for joint set orientations refer to Fig. 4 in  
158 Hugentobler et al. (2020)).

159 A thin and patchy recent till layer, surrounding several rock outcrops, covers the lower study area. Due to  
160 the recent glacial retreat, no noteworthy vegetation is present in the study area. The Moosfluh instability, a  
161 well-documented deep-seated gravitational slope deformation (DSGSD) with superimposed shallower rock-  
162 slides (Glueer et al., 2020; Glueer et al., 2019), is situated in the southwest of the study area.

163 The glacial history of the Great Aletsch Glacier, the largest ice mass in the European Alps, is summarized  
164 in Holzhauser et al. (2005) and glacial extents in the vicinity of the study area have been investigated in  
165 detail by Grämiger et al. (2017). Additionally, glacial retreat from the last local maxima in 1860, the Little Ice  
166 Age (LIA), is well documented by GLAMOS (1881-2019). Since the LIA, the glacier tongue lost more than  
167 3000 m of length and over 300 m in ice thickness at the location of our study site. This leads to a mean ice  
168 height loss of about 2 m per year since LIA. However, annually acquired, high-resolution digital elevation  
169 models of the Great Aletsch Glacier area from the years 2012 until 2019 (source: Swiss Federal Office of  
170 Topography) show that the current melting rates are higher, with about 10 m ice height loss per year.

171



172

173

174

175

176

177

178

Fig. 1. Overview map of the study area at the terminus of the Great Aletsch Glacier at the Autumn 2017 ice extent with the research borehole locations B2, B4, and B6 (modified after Hugentobler et al., 2020). The former glacial extents of years 1927 to 2014 were digitized from historical aerial photos by Glueer et al. (2020) and the Little Ice Age (LIA) and Egesen maximum extents are well constrained by lateral moraines in the map area. We extended the geological map from Steck (2011) in the area that had been glacier covered during their mapping campaign. The numbered solid black lines are the extents of the 2D profiles used for the numerical study.

179

## 2.2. Subsurface monitoring system and previous work

180

181

182

183

184

In summer 2017, a subsurface monitoring system has been installed to investigate and quantify the effects of thermo-hydro-mechanical rock slope processes that occur along with downwasting and retreat of glacial ice (Hugentobler et al., 2020). The monitoring system is installed in three vertical, 44 to 50 m deep instrumented boreholes specifically drilled for research purposes and containing a diameter of 10 cm (B2, B4, and B6, see Fig. 1). The study site is considered as representative for many recently deglaciated rock slopes

185 in inner Alpine valleys with its moderately to steep dipping slope, a crystalline lithology intersected by slope  
186 subparallel joints and alpine tectonic joint sets and faults. Similar geological preconditioning factors can be  
187 found in very many Alpine valleys, and presumably also in many other young mountain belts, such as the  
188 Himalaya and Southern Alps. The three borehole locations were selected to have varying lateral distance  
189 to the glacier margin, so that they monitor the rock slope conditions at different timings relative to deglacia-  
190 tion (Fig. 1), and in slope sectors of different degree of stability and damage. Before the recent deglaciation,  
191 the borehole locations were ice covered for approximately 2000 to 3000 years (Holzhauser et al., 2005).  
192 The location of borehole B2 was for the first time uncovered in summer 2017, and the glacier returned in  
193 winter 2018 for about 4 month (cf. Hugentobler et al., 2020). According to high resolution aerial images  
194 (source: Swiss Federal Office of Topography), the borehole locations B4 and B6 were uncovered from gla-  
195 cial ice in summer 2014 and summer 2016, respectively. Current ice melting rates caused an ice height loss  
196 of about 30 m at our study site during the three years of monitoring.

197 The boreholes are fully grouted, and contain high resolution vertical FBG (fiber Bragg grating) strain sensors  
198 and SAA (shape accel array) in-place inclinometers for the measurement of horizontal deformation, a tem-  
199 perature sensor chain, and a pore pressure sensor installed in a 1 – 2 m long sand filter at the borehole end  
200 (see Fig. 2). The setup and performance and early data of the monitoring system is described in detail in  
201 Hugentobler et al. (2020). Grouting strain sensors into boreholes is the state-of-the-art procedure to couple  
202 the sensors with the formation (Choi et al., 2021) and the grouting was conducted by a specialist company  
203 for geotechnical monitoring. The grout volume as well as strain and temperature in the borehole was moni-  
204 tored during the grouting process to assure a complete filling of the boreholes.

205 Air temperature is measured at our study site with a 30 min interval and total precipitation data used in this  
206 study is provided by MeteoSchweiz and recorded at the weather station “Bruchji” (canton Valais) located  
207 about 6 km away from our study site. Most intense precipitation events recorded at the Bruchji station during  
208 our monitoring period could be also confirmed at our study site by a specific seismic noise response meas-  
209 ured at a seismic sensor installed at the study site by Manconi et al. (2018). We therefore think that it is  
210 reasonable to use the data of this weather station for our analysis.

211 The rock mass and the hydrogeological properties at our study site have been characterized with surface

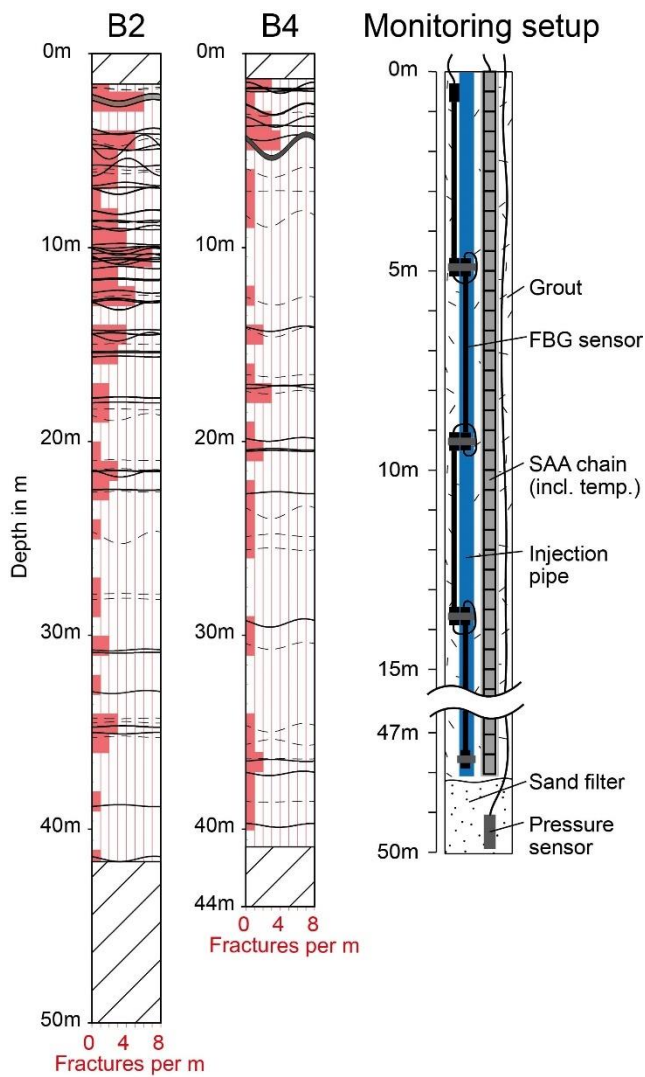
212 structural mapping, rock mass classifications (at outcrops surrounding the borehole sites and from borehole  
213 optical televiewer images), borehole geophysical and hydro-geophysical investigations, as well as pumping  
214 and injection tests in the boreholes. These analyses have identified differences between the three research  
215 borehole locations (Hugentobler et al., 2020). The main findings for the individual boreholes related to rock  
216 mass quality are summarized below. References to the glacier position refer to those present during the  
217 year of drilling (2017).

218 Borehole B2 was drilled directly at the ice margin at the end of a relatively flat plateau and only about 200  
219 m away from the active Moosfluh slope instability. Optical televiewer images of the borehole wall revealed  
220 a high fracture density with open joints often filled with fines in the uppermost 20 m (Fig. 2). Below this  
221 depth, fractures occur less frequently and with lower aperture. The rock mass at outcrops surrounding B2  
222 was classified with a Geological Strength Index (GSI) between 55-65. According to the optical televiewer  
223 image, these values can be confirmed for the upper part of the borehole, but slightly increase with depth  
224 due to the decreasing fracture density (Fig. 2). From a borehole water injection test, the transmissivity in the  
225 lower part of the borehole (around 15 to 50 m depth) was estimated around  $10^{-6}$  m<sup>2</sup>/s and in the uppermost,  
226 fractured part around  $10^{-3}$  m<sup>2</sup>/s.

227 Borehole B4 is located about 50 m away from the glacier margin at a relatively evenly dipping slope. Bore-  
228 hole optical televiewer logs show that the rock mass is less fractured compared to B2 (Fig. 2), with mainly  
229 closed or low aperture structures. A surficial layer of about 5 m with a dense fracturing is present at this  
230 location (Fig. 2). GSI values at outcrops around B4 reveal a high-quality rock mass with values between 75  
231 and 85. Similar to B2, the rock mass quality appears to increase with depth with the observed decrease in  
232 fracture density. A pumping test in the borehole revealed a transmissivity of about  $10^{-6}$  m<sup>2</sup>/s between 9 and  
233 44 m depth and higher assumed values in the uppermost section. Fluid electric conductivity logs show a  
234 major transmissive structure at the depth of 29.4 m and minor transmissive structures at 19.5 m, 25 m, and  
235 39.8 m.

236 Borehole B6 was drilled at a cliff position with about 5 m lateral distance to the glacier margin. The area  
237 around the borehole is characterized by a disturbed rock mass bounded by a prominent head scarp above  
238 (see Fig. 1). Surface structural mapping indicates that this area is likely an inactive toppling rock slope

239 instability, hosting important groundwater springs. We estimated GSI-values at outcrops around B6 to range  
240 between 50 and 60. Because of unstable borehole conditions, a perforated PVC casing was installed in the  
241 borehole (cf. Hugentobler et al., 2020). Therefore, only fluid electric conductivity logging and a pumping test  
242 could be conducted. These tests resulted in an estimated borehole transmissivity of around  $10^{-5}$  m<sup>2</sup>/s with  
243 higher assumed values in the top layer and major transmissive structures at a depth of 35.5 m and 43 m. A  
244 surface creek that originates from springs located a few tens of meters above the borehole location passes  
245 a depression next to the borehole and was observed to infiltrate through fractures into the borehole during  
246 drilling works. The lower GSI-values, the higher transmissivity, and the borehole stability issues encountered  
247 while drilling reveal the lower rock mass quality at this borehole location compared to the other two.



248

249 *Fig. 2. Illustration of structures mapped on the optical televiewer image in borehole B2 and B4 and a conceptual sketch*  
 250 *of the monitoring setup in the boreholes (modified after Hugentobler et al., 2020). An optical televiewer image of B6*  
 251 *does not exist because no such survey could be conducted in this borehole. Solid black lines in the structure logs*  
 252 *indicate major discontinuities such as open joints, filled joints, sheared and fractured zones. Dashed lines indicate minor*  
 253 *discontinuities (e.g., closed or healed joints). Red bars show the fracture count per m along the borehole. Hatched black*  
 254 *areas in the structure logs indicate depth sections with no optical televiewer data and vertical red reference lines are*  
 255 *related to the fracture count per meter.*

## 256 3. Methods

### 257 3.1. Analysis of monitoring data

258 In this paper, we present a detailed analysis of data from the subsurface temperature sensor chains, as well  
259 as from the high resolution vertical FBG strain sensors. Horizontal strain data from the SAA in-place incli-  
260 nometer system is not discussed in detail due to space reasons but is provided in section 5.3 (Fig. 12) to  
261 support our discussion on the overall observed strain characteristics and its implications for paraglacial rock  
262 slope evolution. Subsurface temperatures have been recorded since October 2017 with an hourly measure-  
263 ment interval, and a downhole sensor spacing of 1 m. Some data gaps of a few weeks in total exist in the  
264 time series that are related to battery issues. One longer data gap of four months (April to July 2018) in the  
265 B2 time series is related to a temporary glacier re-advance that overran the borehole location and disrupted  
266 the loggers from the sensor chains.

267 We use the subsurface temperature data to empirically estimate the in-situ apparent thermal diffusivity  $D$   
268 within the annual thermally active layer.  $D$  is defined as  $D = \lambda/(\rho C_p)$ , where  $\lambda$  is the thermal conductivity,  $\rho$   
269 the density of the rock mass, and  $C_p$  the specific heat capacity of the rock. This was done by analytically  
270 solving the 1D heat conduction equation for measured periodic surface temperature cycling, and fitting our  
271 subsurface temperature data (cf. Koo and Song, 2008; Rajeev and Kodikara, 2016; Schneider et al., 2012).

272 In this analysis, annual surface temperature variations are approximated as periodic oscillations and ex-  
273 pressed as Fourier series, which are then used as boundary conditions to solve the 1D (vertical to ground  
274 surface) heat conduction equation. From the resulting analytical solution with time-periodic surface temper-  
275 ature variations in a semi-infinite half-space, equations for phase delay (linear trend with depth) and ampli-  
276 tude decay (exponential decay with depth) can be derived (Eqn. 13 and 14 in Rajeev and Kodikara, 2016).  
277 These equations were then inverted to calculate the thermal diffusivity from the phase delay and amplitude  
278 decay of the annual temperature wave penetrating the subsurface at our borehole sites.

279 To estimate the phase delay, we applied a cross-correlation analysis between the temperature readings at  
280 the uppermost sensor and each other sensor in depth. The amplitude ratio between two time series recorded  
281 at different depths was calculated by first aligning the time series using the phase difference from the cross-

282 correlation analysis and then performing a linear regression analysis between the two aligned temperature  
283 time series. The slope of the linear regression equals the amplitude ratio. We used these results to interpret  
284 which borehole locations are conduction dominated, as well as to parametrize our 2-D continuum heat  
285 transfer models.

286 The FBG sensors are installed as a serial connection of ten individual sensors with base lengths of 4 to 5  
287 m and cover the full length of each borehole (see Fig. 2). The principles of operation of FBG strain sensors  
288 are described in detail in the literature (Morey et al., 1990; Zhu et al., 2017). The individual strain values  
289 were calculated by averaging over hourly dynamic measurements of approximately 30 s duration. In  
290 Hugentobler et al. (2020) we introduced the strain signals measured with the FBG-system and showed that  
291 the system is capable of reliably detecting strains with a precision below  $1 \mu\epsilon$  (or  $4 \mu\text{m}$ ).

292 The individual FBG strain sensors show long term continuous changes in strain (positive strains equal ex-  
293 tension and negative strains contraction of the monitored base length), distinct short-term strain events  
294 (within hours to days), and rapid strain steps (within one measurement cycle of 1 h) (Fig. 6, Fig. A 1, A 2,  
295 and A3). We compared the strain time series of the individual sensors in all three boreholes to variables of  
296 potential drivers for deformation (precipitation, pore pressures, surface temperature). Additionally, we ap-  
297 plied an event detection procedure to specifically investigate drivers for short-term and rapid strain variations  
298 (hereafter called strain events). An explanation of the different strain signals is provided in the beginning of  
299 section 4.1.3.

300 To investigate potential drivers for strain events in the data and their distribution over the year, the timing of  
301 the most significant strain events in the time series were automatically retrieved using a MATLAB-based  
302 function. This function finds the most significant change points in a time series based on statistical properties  
303 (in our case mean and slope) and a predefined maximum number of change points (Killick et al., 2012;  
304 Lavielle, 2005). The function proceeds in the following steps: (1) Choose a division point in the time series  
305 and divide it into two sections; (2) Compute an empirical estimate of the desired statistical property (in our  
306 case mean and slope) for both sections; (3) Measure the deviation between the empirical estimate and each  
307 point in the section and add the deviations for all points; (4) Add the deviations section-to-section to find the  
308 total residual error; (5) Vary the location of the division point until a minimum total residual error is found. A

309 maximum number of 50 changing points per strain time series were defined by trial and error for both the  
310 mean and slope criterion and their results were intersected because this yielded the best results. With this  
311 approach we did not detect every single strain event but sampled the most significant strain events present  
312 in the time series. All automatically detected strain events were then manually checked. A minority of de-  
313 tected events were corrected because they were artifacts related to data gaps, but the majority could be  
314 confirmed.

315 The timing of these most significant strain events was then compared to the potential drivers for deformation.  
316 We expect that the drivers of strain events may be depth dependent because annual surface temperature  
317 cycles mainly affect the shallow subsurface and hydromechanical effects related to pore pressure fluctua-  
318 tions are expected to be more important at greater depth (i.e., below the phreatic groundwater surface of  
319 the slope). Therefore, we distinguish deep and shallow strain events. This allows us to analyze the different  
320 drivers of short term and rapid strain events, which are potentially related to rock mass damage.

## 321 3.2. Numerical simulation

322 We performed 2D, finite-element (FE) numerical modeling in order to understand long term (on the order of  
323 200 years) changes of the slope thermal regime caused by glacial retreat, as well as yearly changes in the  
324 thermal regime, and resulting thermo-elastic strain, driven by seasonal temperature cycles. 2D numerical  
325 simulations were conducted using the commercial finite element software COMSOL Multiphysics v 5.5. The  
326 model geometry was defined using 2D cross-sections that intersect the three borehole sites, and laterally  
327 extend from the glacier-filled valley bottom to the ridge of Moosfluh/Hohfluh (see Fig. 1). Surface topography  
328 above the current glacial ice level was defined using a high-resolution DEM from 2018 of the study area  
329 (source: Swiss Federal Office of Topography). Elevations of bedrock sections currently covered by glacial  
330 ice were interpolated using data from Rutishauser et al. (2016) in GlaThiDa\_Consortium (2019).

331 To allow a comparison with monitored temperature and strain data recorded in our rock slope at high spatial  
332 resolution, we used a triangular FE mesh geometry with two domains (see Fig. 3). Domain 1 covers the  
333 surrounding of the borehole locations and is composed of a fine mesh with element sizes between 0.03 m  
334 and 18 m and increasing mesh size with normal distance to the ground surface. This resulted in individual  
335 mesh sizes of a few centimeters to maximum a few decimeters along the 50 m deep modeled borehole.

336 Domain 2 contains a coarser mesh with mesh sizes between 0.5 m and 95 m and an increase of mesh size  
337 with normal distance to ground surface and Domain 1.

338 Heat conduction is the only heat transfer process occurring in these continuum models and our models  
339 solve the heat conduction equation defined as  $\partial T / \partial t = D \nabla^2 T$  for the model domain. The thermal diffusivity  
340  $D$  is mainly based on the empirical estimations described in the previous section, and the  $C_P$  and  $\rho$  values  
341 used in the 2D model are based on literature values, as summarized in Table 1. We used a depth dependent  
342 thermal diffusivity in our models to partially account for the depth dependent structural heterogeneity present  
343 at our study site. Between 0 and 10 m depth we assigned the mean estimated in-situ value based on the  
344 inversion procedure detailed above. From 20 m downwards a constant literature value for intact rock thermal  
345 diffusivity was used (Table 1), and in between these two values the thermal diffusivity was linearly interpo-  
346 lated. The transient subsurface temperature field in the model was calculated by assigning boundary con-  
347 ditions (BC) of a constant geothermal heat flux at the bottom, a transient surface rock temperature at the  
348 top (described in more detail below), and no-flow lateral boundaries (Fig. 3). To achieve a realistic geother-  
349 mal gradient of  $\sim 23 \text{ }^\circ\text{C km}^{-1}$  in depth (cf. Rybach and Pfister, 1994), the geothermal heat flux at the bottom  
350 boundary of the model was set to  $60 \text{ mW m}^{-2}$  which agrees to values used in literature (Wegmann et al.,  
351 1998).

352 *Table 1. Literature parameters used for the numerical simulations.*

<i>Thermal properties</i>		
<i>Specific heat capacity <math>C_P</math> (at constant pressure)</i>	780 J kg <sup>-1</sup> K <sup>-1</sup>	Wegmann (1998)
<i>Thermal conductivity <math>\lambda</math> (intact rock)</i>	2.9 W m <sup>-1</sup> K <sup>-1</sup>	Wegmann et al. (1998)
<i>Mechanical properties</i>		
<i>Density <math>\rho</math></i>	2700 kg m <sup>-3</sup>	Wegmann et al. (1998)
<i>Poisson's ratio</i>	0.2	Grämiger et al. (2017)
<i>Young's modulus</i>	30 GPa	Grämiger et al. (2017)
<i>Thermal expansion <math>\alpha</math></i>	$9.5 * 10^{-6} \text{ K}^{-1}$	Keusen and Amiguet (1987)

353

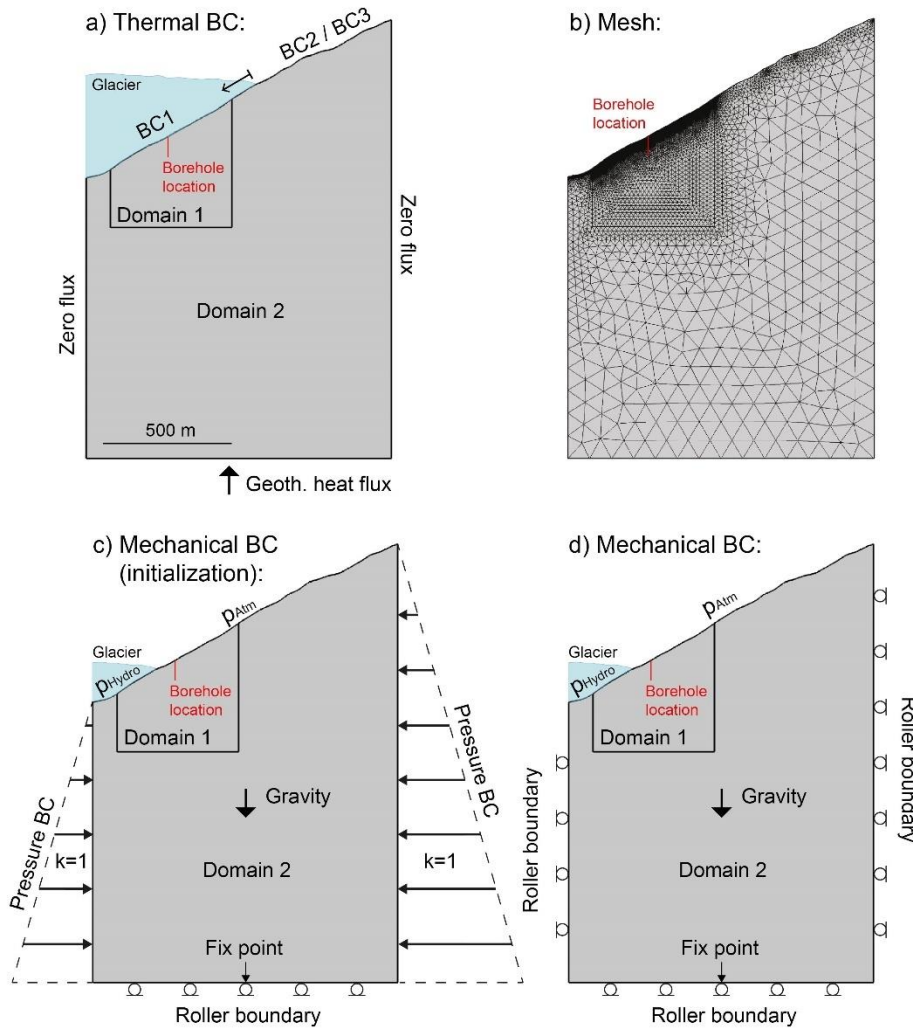
354 The numerical modeling was performed in four steps, with the different boundary conditions visualized in  
355 Fig. 3 and the thermal boundary conditions detailed in Table 2:

- 356 1. The steady-state subsurface temperature field was calculated for the LIA ice extent (see Fig. 9a) using  
 357 0° C at the top boundary below ice elevation (BC1) and above the ice elevation an elevation depend-  
 358 ent mean annual ground temperature (MAGT) function (BC2).
- 359 2. Starting from the steady-state temperature field of modeling step 1, a transient model was run to simu-  
 360 late the thermal effect of the lateral ice retreat from the LIA (~1860) to the 2017 ice extent. Historical  
 361 aerial photos show that the lateral ice retreat along our modeled profiles correlates linearly with the  
 362 documented glacier length change of the Great Aletsch Glacier (GLAMOS, 1881-2019), which has  
 363 been monitored in detail. Therefore, we used the rate of glacial length change to calculate the lateral  
 364 ice extent in each time step of the model. With this method, the modeled timing of deglaciation at the  
 365 borehole locations deviate by a maximum of 2 years compared to the actual year of deglaciation. A  
 366 constant temperature of 0° C (BC1) was assigned to the part of the top boundary below this lateral ice  
 367 extent, and an elevation dependent MAGT function (BC2) was assigned above.
- 368 3. Following the simulation of ice retreat from the LIA, seasonal temperature variations were modeled  
 369 using the measured temperature recorded at the uppermost sensor of borehole B4 (BC3), superim-  
 370 posed on the long-term deglaciation trend since LIA. In this modeling step, the temporal resolution  
 371 was increased to 1 hour in order to investigate the effects of seasonal temperature cycles on the sub-  
 372 surface temperature field. Similar to modeling step 1 and 2, BC1 was assigned at the top boundary  
 373 below glacial ice. To achieve the best possible fit of the initial conditions with measured temperatures  
 374 in borehole B4 we varied the model parameters for modeling step 2 (LIA retreat) by using a constant  
 375 intact rock thermal diffusivity of  $1.4 \cdot 10^{-6} \text{ m}^2/\text{s}$  instead of the 2-layer thermal diffusivity. Then modeling  
 376 step 2 was run for 158 years (1860 (LIA) to 2018). Following this, we applied a spin-up period of one  
 377 annual cycle using again the 2-layer thermal diffusivity and BC3 top condition (Table 2) to allow the  
 378 models' initial conditions to equilibrate with the boundary conditions. For the simulation of the sea-  
 379 sonal temperature cycles we then used the 2-layer thermal diffusivity introduced above.

380 *Table 2. Used thermal boundary conditions (BC) to model 2D heat conduction in our glacier adjacent rock slopes.*

BC #	Description	Value	Notes
BC1	Temperature below ice elevation	0° C	Elevation dependent gradient adapted from Grämiger et al. (2018)
BC2	MAGT above ice elevation	$\text{MAGT}(z)=12.55-0.005 \cdot z$ [°C]	

381



382

383 Fig. 3. Visualization of the model geometry (drawn to scale), thermal BC (a), finite element mesh (b), and mechanical  
 384 BCs (c and d) used for the numerical simulations. BC1, BC2, and BC3 are described in Table 2.

- 385 4. Following the thermal modeling steps 1 to 3, we computed the expected thermoelastic strains result-  
 386 ing from seasonal surface temperature cycles measured at our site using partially coupled thermome-  
 387 chanical numerical simulations. The simulations are partially coupled because temperature changes  
 388 influence stresses, but stress changes do not influence thermal boundary conditions, thermal proper-  
 389 ties, or the temperature field. We used a simplified continuum modeling approach and homogenous

390 and isotropic elastic rock mass properties, following Grämiger et al. (2017) (see Table 1). The thermo-  
391 mechanical modeling was conducted in two steps using the same model geometry as for the thermal  
392 models. First, we initialized the stresses in the rock slope with a steady-state simulation applying me-  
393 chanical forces only. Far-field stresses that are of tectonic and exhumation-induced origin were mod-  
394 eled in a simplified way with a horizontal to vertical stress ratio of  $k=1$  (Kastrup et al., 2004) at the lat-  
395 eral boundaries of the model (Fig. 3c). We applied a roller boundary (i.e., constrain the displacement  
396 in direction normal to the boundary) at the bottom and a fix point constraint (i.e., no displacement at  
397 this point) at the center of this boundary line to keep the model in place. In addition, we added gravity  
398 and modeled a constant glacier load at the 2017 ice extent as a hydrostatic stress boundary (cf.  
399 Grämiger et al., 2017). After initialization, we switched the lateral mechanical boundaries to roller  
400 boundaries (see Fig. 3d) and calculated the thermal modeling step 3 including a thermomechanical  
401 coupling through the thermal expansion coefficient  $\alpha$ . We used the same thermal initial and boundary  
402 conditions as described in modeling step 3.

## 403 4. Results

### 404 4.1. Subsurface monitoring data

#### 405 4.1.1. Temperature data

406 Fig. 4 shows the subsurface temperature evolution of the glacier adjacent rock slope from 2018 to 2020 at  
407 the three borehole locations. The graphs in the three first columns of the figure (a, b, c, e, f, g, i, j, k) show  
408 the annual temperature variation in the form of monthly mean temperature profiles, and the graphs in the  
409 column to the right of the figure (d, h, l) show the evolution of the annual mean temperatures of the three  
410 monitored years. Since we started to monitor the temperature in fall 2017, our provided annual temperature  
411 cycles start in November and end in October of the following year (e.g., 2018 contains data from Nov. 2017  
412 until Oct. 2018). Fig. 4 shows that the depth of the thermally active layer in B2 and B4, is around 17 m, and  
413 annual temperature cycles smoothly diffuse into the subsurface. In contrast, in borehole B6 the annual ther-  
414 mally active layer is around 28 m deep, and the temperature profile is highly irregular. All three boreholes  
415 show weak positive and negative temperature anomalies along the profile.

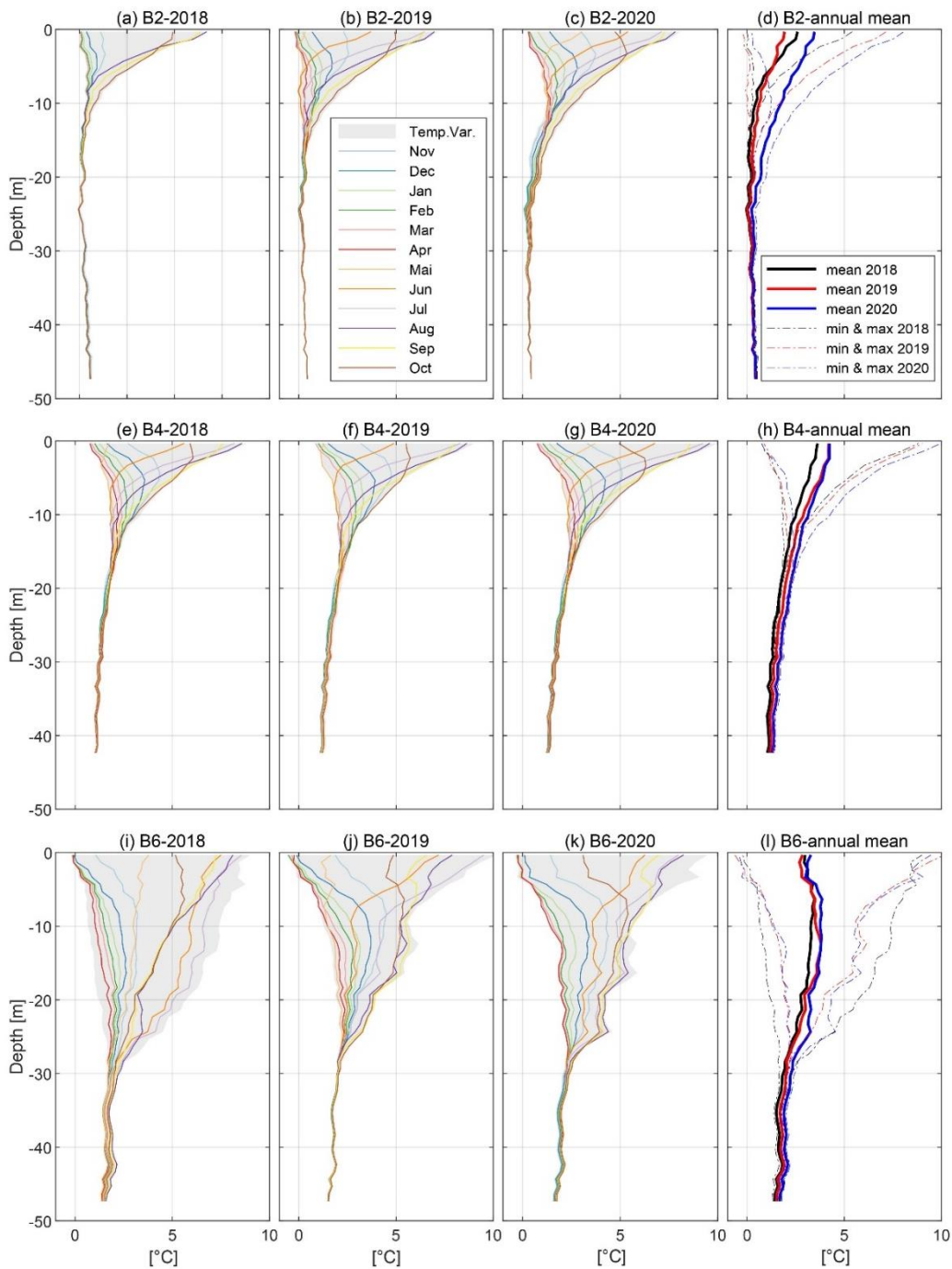
416 Borehole B2 is the closest of the three boreholes to the glacier margin, and shows the lowest mean surface  
417 temperature in 2018 and a clear warming trend in the two following years. This warming trend is likely related  
418 to the significant change of distance to the glacial ice at this borehole location (from 0 m in 2017 to about  
419 40 m in 2020). The annual variability in this borehole is around of 7 to 8 °C at the uppermost sensor. B4,  
420 which is the borehole located furthest from the glacier, shows a mean surface temperature of around 4 °C  
421 with an annual variability of around 8 to 9 °C. B6 has an intermediate distance to the glacier, and shows an  
422 annual mean surface temperature of around 3 °C and a variability of around 9 °C. All three boreholes display  
423 a general warming trend, which can be observed as a shift in positive direction of the mean annual temper-  
424 ature profiles between 2018 and 2020 (Fig. 4d, h, l). This warming trend can be overprinted by annual  
425 temperature variations in the uppermost borehole sections (e.g., boreholes B2 and B6).

426 The slopes of the mean annual temperature profiles in the three boreholes reveal that the warming front has  
427 propagated to different depths in each of the three boreholes. Starting with B2, Fig. 4d shows a negative  
428 temperature gradient (i.e., cooling downwards) to a depth of about 17 m (in 2018 and 2019). Between 17  
429 m and 25 m, the temperature during these years were anomalously low, with measured values around 0 °C  
430 in years 2018 and 2019, and showing a clear increase in 2020. Below 25 m the temperature increases with  
431 depth with a gradient of about 0.2 °C / 10 m (i.e., similar to the assumed geothermal gradient of 23°/km in  
432 the area (Rybach and Pfister, 1994)).

433 In B4, the temperature profile (Fig. 4h) shows a cooling downward gradient along the whole length of the  
434 borehole, although this gradient reduces with depth. This reduction indicates that the trend may switch to  
435 warming downward below the borehole depth, similar to the trend observed in B2 below 25 m.

436 Borehole B6 shows a general temperature decrease with depth below a depth of 10 m, but with a more  
437 irregular shape of the temperature profile showing deviations in positive and negative directions. It is im-  
438 portant to mention that the upper 27 m of borehole B6 were not grouted until August 2018, because signifi-  
439 cant quantities of grout were lost through transmissive structures during the initial campaign in October 2017  
440 (cf. Hugentobler et al., 2020). The open borehole and the exothermal reaction during the second grouting  
441 campaign in August 2018 influenced the B6 temperature measurements in the upper 27 m in 2018. Never-  
442 theless, 2019 and 2020 measurements of this borehole are considered to reflect the undisturbed in-situ

443 subsurface temperatures at this location.



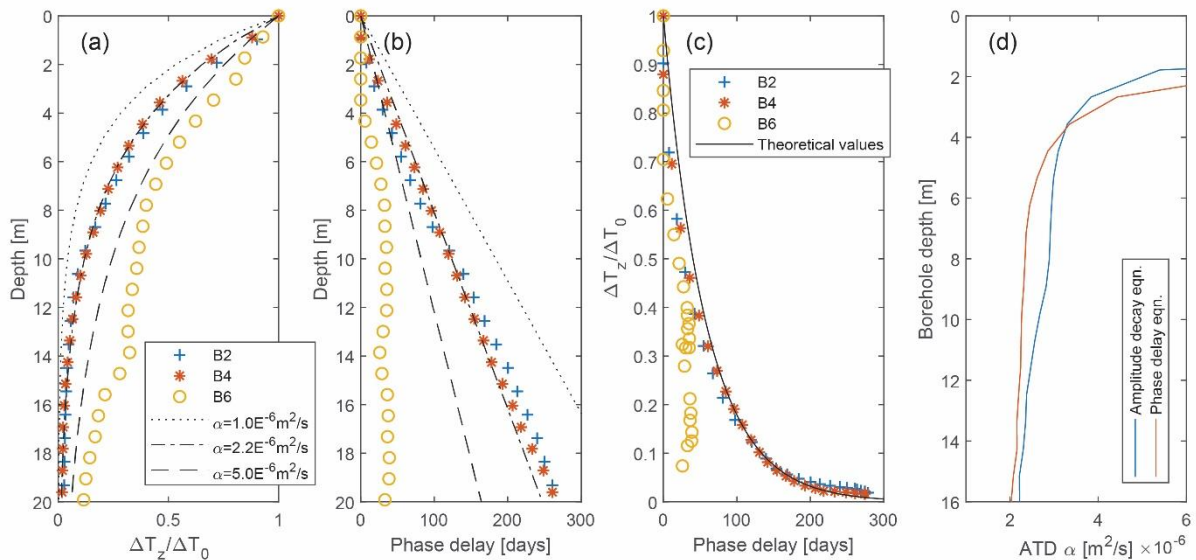
444

445 *Fig. 4. Borehole temperature monitoring data of years 2018, 2019, and 2020 provided as monthly mean temperature*  
446 *profiles (colored lines) for the three research boreholes (B2: plots a, b, c; B4: plots e, f, g; B6: plots i, j, k). The annual*  
447 *temperature variability is illustrated in gray in the background. An annual temperature cycle presented in these plots*

448 contains monthly mean temperatures starting from November of the previous year and end in October of the year pro-  
 449 vided in the respective title. Plots d, h, l show the annual mean temperatures of years 2018, 2019, and 2020, as well  
 450 as the minimum and maximum temperatures measured at each depth, for all the three boreholes.

#### 451 4.1.2. Thermal diffusivity

452 Fig. 5 shows the results of the thermal diffusivity inversion based on periodic annual temperature cycles  
 453 measured during 2019, which include separate estimates based on amplitude decay (Fig. 5a), phase delay  
 454 (Fig. 5b), and their theoretical relationship (Fig. 5c). These results show a regular amplitude damping and  
 455 phase delay with depth in boreholes B2 and B4, while B6 shows strong deviations from the one-dimensional  
 456 heat diffusion model. Fig. 5c also shows that the annual temperature signal measured in B2 and B4 plots  
 457 closely on the theoretical line, suggesting that conductive heat transfer dominates in these two boreholes.  
 458 Temperature data measured in borehole B6 does not follow this theoretical relationship, hence, nonconduc-  
 459 tive processes clearly dominate the subsurface thermal regime in the upper 20 m of this borehole.



460

461 Fig. 5. The plots a, b, and c show the annual variation of the subsurface temperature driven by periodic surface temper-  
 462 ature variations. The black, dashed, dotted, and solid lines correspond to theoretical values calculated from an analytical  
 463 solution of the one-dimensional heat conduction equation for a number of apparent thermal diffusivity values  $\alpha$ . The  
 464 colored markers in the plots indicate the annual temperature variations monitored in our research boreholes in year  
 465 2019. (a) Amplitude decay of a periodic annual thermal signal vs. depth to ground surface. (b) Phase delay of a periodic

466 *annual thermal signal vs. depth to ground surface. (c) Relationship between phase delay and amplitude decay. (d)*  
467 *Estimated apparent thermal diffusivity over depth for borehole B4 data using the 1-D heat conduction equation. The*  
468 *blue line corresponds to the estimation using the amplitude decay in the measured temperature data. The red line*  
469 *corresponds to the estimation using the phase delay in the measured temperature data. The apparent thermal diffusivity*  
470 *values represent the estimates from the depth interval between the uppermost sensor and the given depth in the y-axis.*

471 The best fit values for the mean apparent thermal diffusivity are  $2.1 \cdot 10^{-6}$  m<sup>2</sup>/s for B2 and  $2.2 \cdot 10^{-6}$  m<sup>2</sup>/s for  
472 B4, respectively. Around B4, the slope shows a relatively constant dip angle, so the 1-D approach is likely  
473 more reliable at this location compared to B2, where 2-D effects are assumed to play a more important role.  
474 Therefore, the apparent thermal diffusivity estimate of B4 was used for further investigations.

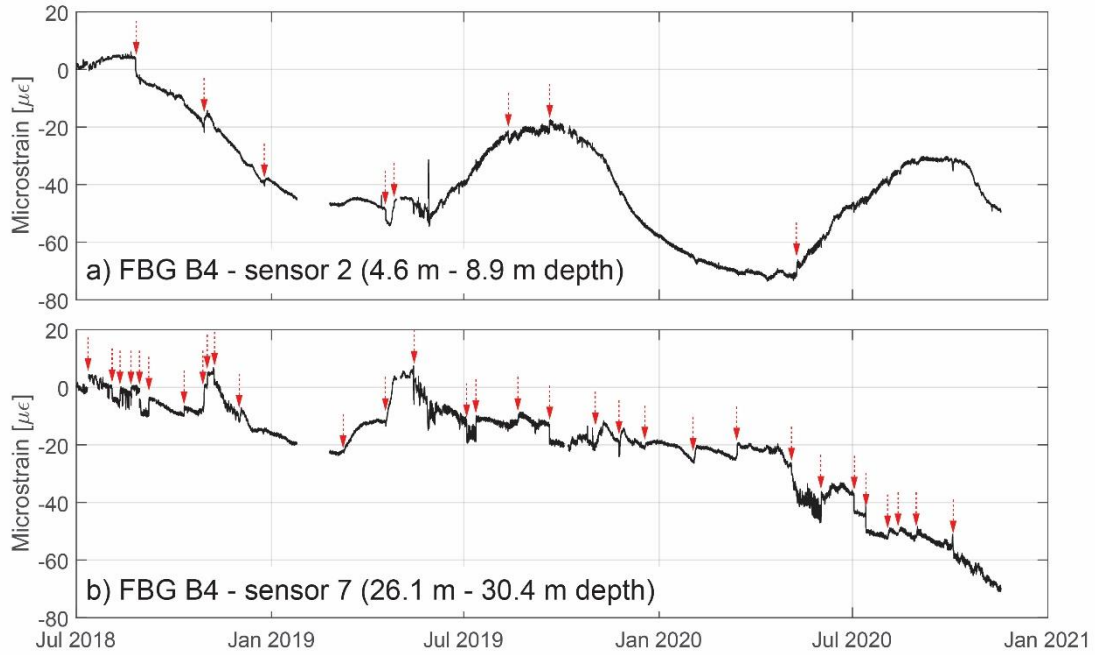
475 Fig. 5d shows the inverted depth dependent apparent thermal diffusivity for B4, based on both the amplitude  
476 decay and phase delay. The estimates from both methods show a similar trend, with decreasing apparent  
477 thermal diffusivity values with depth. The highest values occur in the uppermost 4 m and below a more  
478 gentle decrease with depth is observed. The estimated magnitudes of thermal diffusivity are higher than  
479 literature values for conductive heat transfer in intact gneissic rocks would suggest ( $\sim 1.4 \cdot 10^{-6}$  m<sup>2</sup>/s)  
480 (Wegmann et al., 1998; Wegmann, 1998). We expect the estimated apparent thermal diffusivity values  
481 within the thermally active layer to approach a more constant value close to the intact rock thermal diffusivity  
482 at greater depth. Hence, the higher estimated value is assumed to be an ‘apparent’ value that also com-  
483 prises effects related to the increased fracture density and water / air content in the surficial layer that allow  
484 minor nonconductive processes to occur. Such minor nonconductive effects should not be confused with  
485 stronger advective heat transfer processes, which are likely important in B6 and can result in significant  
486 disturbances of the diffusive profile (e.g., Ge, 1998).

#### 487 4.1.3. FBG vertical strain

488 We recorded both short- and long-term strain signals with the FBG monitoring system. Two characteristic  
489 examples of strain time series are provided in Fig. 6, and the complete FBG strain time series of all sensors  
490 in the three boreholes including variables of potential drivers for deformation are provided in the Appendix  
491 (Fig. A 1, A 2, and A 3).

492 These strain types, which can be identified in all boreholes are: (i) multi-annual trends in strain that mainly

493 occur in negative direction (e.g., Fig. 6a and b), (ii) annual strain cycles (e.g., Fig. 6a), (iii) rapid and short  
494 term strain events typically showing magnitudes of up to around  $20 \mu\epsilon$ , occur in positive and negative direc-  
495 tion (e.g., red arrows in Fig. 6), and can be detected with the algorithm explained in Section 3.1.



496

497 *Fig. 6. Time series of two FBG strain signals measured at different sensors in borehole B4. The complete strain data of*  
498 *all sensors is provided in the Appendix (Fig. A 1, A 2, and A 3). Arrows indicate the timing of short-term and rapid strain*  
499 *events referred to in the text.*

500 A comparison of Fig. A 1 - 3 (Appendix) shows that the strain response at the three borehole locations  
501 varies, but also shows similarities of specific strain signals.

502 In all three boreholes multi-annual negative strain trends (contraction) are observed at several sensors. In  
503 B2 and B6 (Fig. A 1, 3), these negative strain trends are stronger in shallow sensors, while in B4 (Fig. A 2)  
504 they predominate at deeper sensors.

505 The uppermost sensors that monitor strain from around 0 to 5 m depth show an overall positive (extension)  
506 strain trend and some annual cyclic behavior with extension during wintertime and contraction during sum-  
507 mer season.

508 Annual cyclic signals in the opposite direction (i.e., with contraction during the cold wintertime and extension  
509 during the warm summertime) are well visible in FBG-2 and 3 of B4 and are further investigated in section  
510 4.2.3. These signals show a slight phase shift with depth. Similar annual cyclic signals occur in shallow  
511 sensors of B2 and B6 but are less clear because they are superimposed by short-term or rapid strain events  
512 that occur at similar or greater magnitudes.

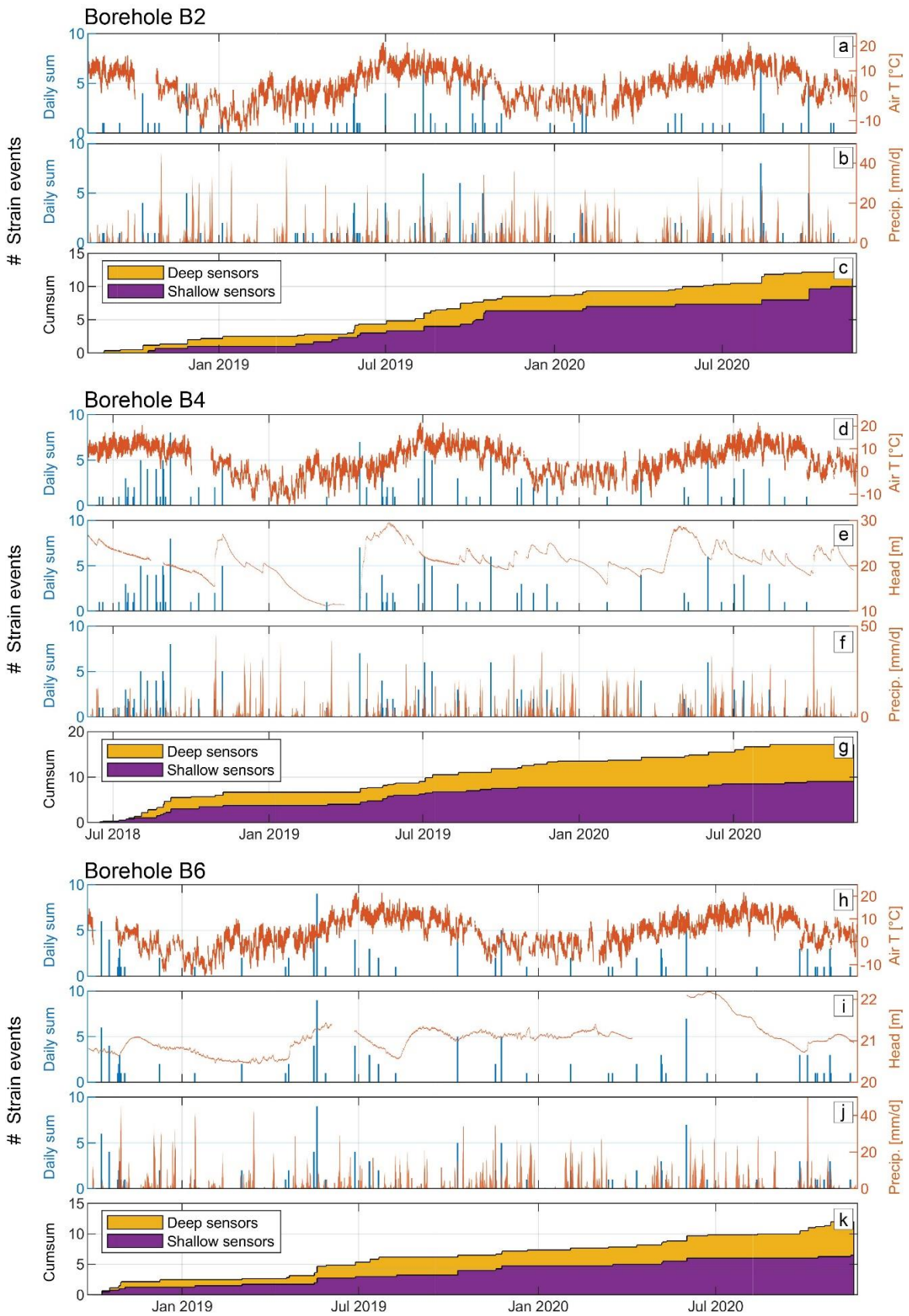
513 These larger strain events with magnitudes between 20 to a few 100  $\mu\epsilon$  occur most frequently in borehole  
514 B2 (Fig. A 1), and could either be significant deformation events, or an artefact of the FBG signal processing.  
515 Most of these steps could either be verified by simultaneous deformation detected with the independent in-  
516 place inclinometer system in the borehole (cf. Hugentobler et al., 2020), occurred at several FBG sensors  
517 simultaneously (b in Fig. A.2), or coincided with potential triggers (e.g., rainfall events or pore pressure  
518 changes; b in Fig. A.1). Hence, they are interpreted as significant deformation events. Only one particular  
519 large step in sensor FBG-4 of borehole B2 (small form letter a in Fig. A 1) is likely a signal processing  
520 artefact and was removed in the analyses that follow. The most significant large magnitude strain event  
521 occurred in B2 at several sensors simultaneously and coincided with an extreme rainstorm event (label b in  
522 Fig. A 1).

523 Fig. 7 presents a comparison of automatically detected strain events of the FBG-sensors with potential  
524 drivers for deformation, including surface temperature, pressure head, and precipitation. Results presented  
525 in Fig. 7 are summarized in the pie plots of Fig. 8, which shows the percentage of the strain events coinciding  
526 with the potential drivers at the specific boreholes. The data shows that, depending on the borehole, be-  
527 tween 60 and 75 % of the strain events coincide with precipitation events (Fig. 7b, f, and j; Fig. 8 Fig. 8).  
528 Only about half of these precipitation events caused a clear pressure head increase (Fig. 7e and i; Fig. 8).  
529 On the other hand, 5 to 9 % of the strain events temporally correlate with pressure head increases not  
530 related to direct rainfall infiltration but to snowmelt infiltration. Very few strain events (< 2 %) coincide with  
531 extreme surface temperatures (Fig. 7a, d, and h; Fig. 8). These results emphasize the importance of hydro-  
532 mechanical and potentially moisture-related processes for deformation. However, the interactions are com-  
533 plex, as rainfall also modifies the mechanical and hydraulic conditions of the adjacent glacier. Analyzing  
534 these complex interactions is beyond the scope of the present paper and are explored in a companion

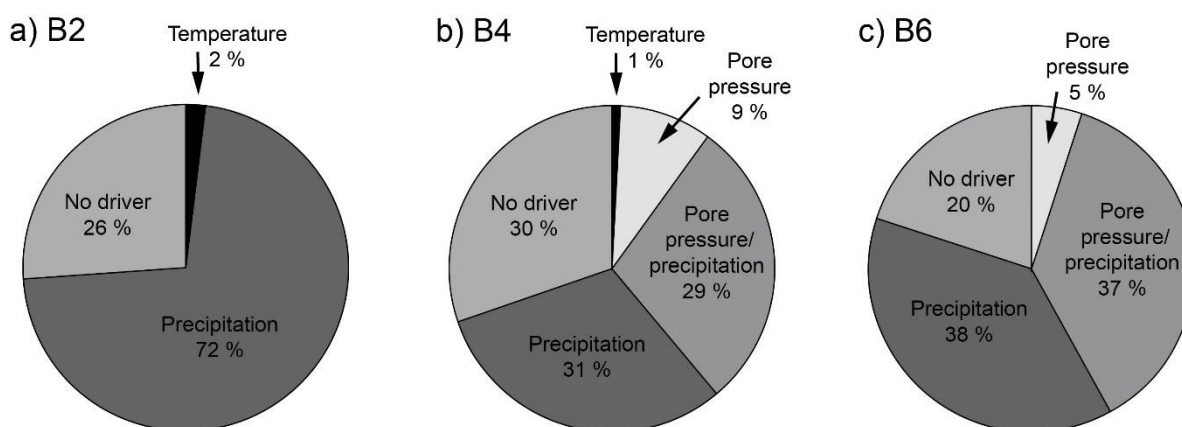
535 paper.

536 Between 20 to 30 % of the strain events do not coincide with any of the three potential triggers. To investi-  
537 gate if these events could be related to earthquakes, which are also frequently discussed as destabilizing  
538 factors during deglaciation (e.g., McColl and Draebing, 2019), we compared the timing of the strain events  
539 with measured earthquakes in the observation period (data provided by the Swiss Seismological Service,  
540 SED). Earthquakes that occurred at epicentral distances less than 50 km from the study site and having  
541 magnitudes greater than M1 and an earthquake depth of less than 15 km were used for the comparison.  
542 However, we did not find any correlation between the around 70 recorded earthquakes during the monitoring  
543 period (maximum magnitude M3) and the measured strain events in our boreholes. A characterization of all  
544 earthquake events used for the comparison (i.e., magnitude, epicentral distance to study site, and earth-  
545 quake depth) can be found in the Appendix (Fig. B 1).

546 The cumulative numbers of detected strain events (Fig. 7c, g, and k) allow us to better visualize the variation  
547 of the number of events occurring over the year. Data in these plots is provided as mean number of strain  
548 events per sensor interval for shallow sensors (within the annual thermally active layer, i.e., the uppermost  
549 ~ 18 m) and for deep sensors (~18 m down to the borehole end). Fig. 7 shows that fewer strain events occur  
550 during wintertime compared to the spring and summer season and that these strain events occur more  
551 frequently in deeper sensors. This difference between shallow and deeper sensors is more strongly pro-  
552 nounced in B4 and B6 compared to B2. In B2, some large magnitude strain events are measured in the  
553 shallow layer (see Fig. A 1, Appendix).



555 Fig. 7. Number of detected strain events during the monitoring period in the three boreholes compared to potential  
 556 drivers for deformation. Panels a, d, h: Daily sum of events vs. air temperature at the study site. Panels e, i: Daily sum  
 557 of events vs. pressure head measured at the borehole end (no functioning pore pressure sensor installed in borehole  
 558 B2). Panels b, f, j: Daily sum of events vs. cumulative total precipitation per 24 h measured around 5 km away from the  
 559 borehole location at the weather station “Bruchji”, canton VS (provided by MeteoSchweiz). Panels c, g, k: Mean cumu-  
 560 lative sum of events per sensor provided for “shallow sensors” (i.e., down to 18 m depth) and “deep sensors” (i.e., from  
 561 18 m down to the borehole end).



562  
 563 Fig. 8. Pie plots for the three boreholes (B2, 4, 6) that summarize the percentage of the automatically detected strain  
 564 events presented in Fig. 7 that coincide with potential drivers such as precipitation, pore pressure changes, or extreme  
 565 surface temperatures. Because no functioning pore pressure sensor is installed in B2, a comparison with this potential  
 566 driver cannot be provided for this borehole.

## 567 4.2. Modeling temperature evolution and deformation during deglaciation

### 568 4.2.1. Temperature evolution since LIA

569 Fig. 9 shows simulated subsurface temperatures during LIA deglaciation compared to our measured mean  
 570 subsurface temperatures at the borehole locations. Fig. 9a shows the temperature field of the steady-state  
 571 solution during the LIA ice extent, which, as mentioned previously, is used as an initial condition for the  
 572 following transient ice retreat simulation. The modeled temperature field in 2019 is shown in Fig. 9b. Fig. 9c  
 573 illustrates the change of the subsurface temperature profile at the specific indicated mid-slope location dur-  
 574 ing glacial retreat.

575 As can be seen on Fig. 9c, the subsurface temperature profile before deglaciation shows 0° C at the ground

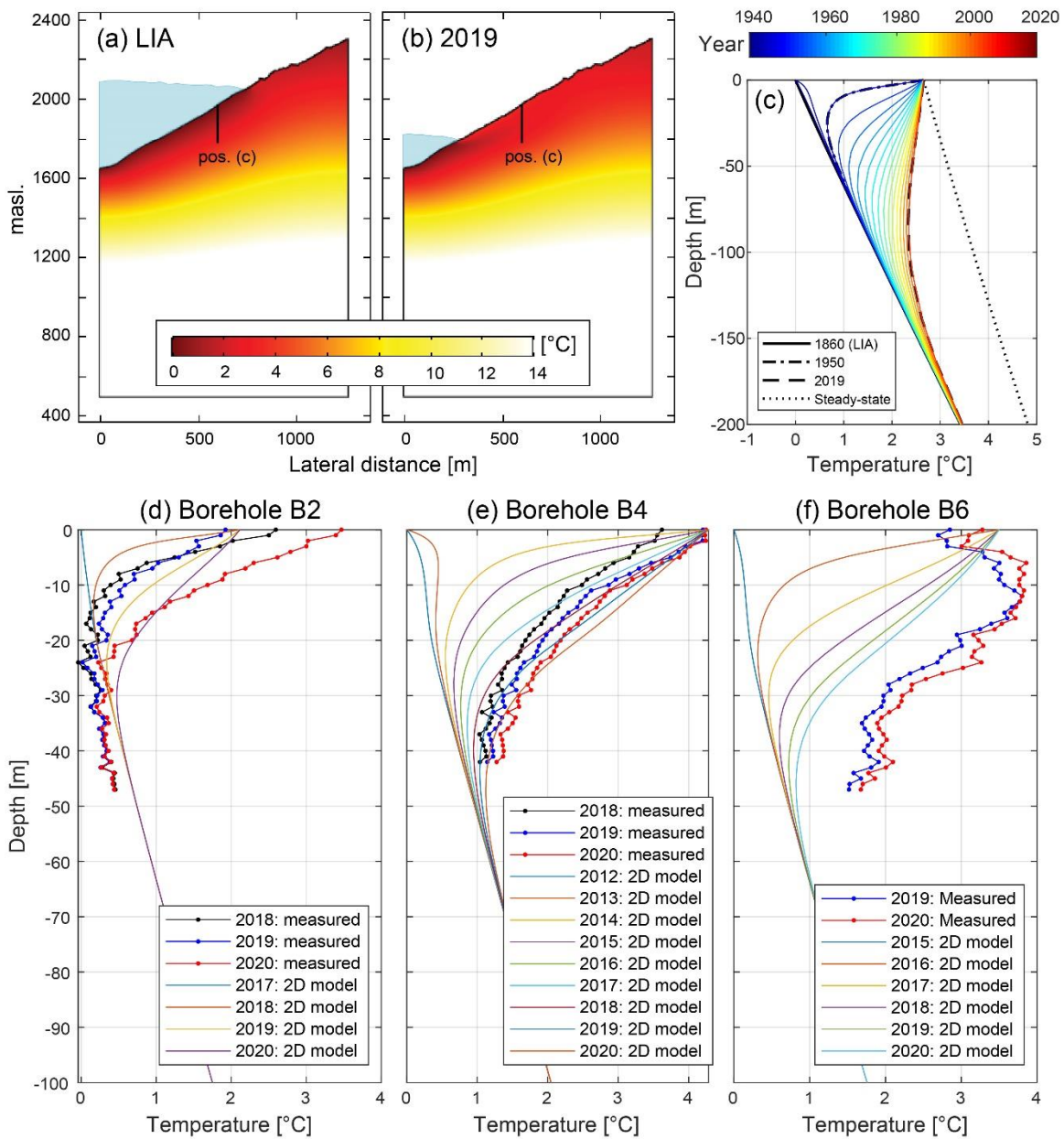
576 surface (BC1 below ice) with a nearly linear temperature increase with depth. As soon as the ice retreats  
577 below position c, a new mean annual ground temperature is applied to the model (BC2 in Table 2) which  
578 results in warmer surface temperatures that penetrate downward with time. The adaption of the subsurface  
579 temperature to a new, warmer MAGT causes a transient inverse gradient in the upper subsurface temper-  
580 ature profile (i.e. cooling downwards), which transitions to a positive geothermal gradient at depth. Hence,  
581 an inverse thermal profile can be an indication for a transient subsurface temperature adapting to a new,  
582 warmer surface temperature (e.g., Pollack et al., 1998). The dashed line in Fig. 9c illustrates a newly ap-  
583 proached steady-state temperature profile assuming the new MAGT of around 2.6° C to be constant over a  
584 very long time at the elevation of the profile. The time required to reach this new steady-state temperature  
585 profile is dependent on the thermal diffusivity of the medium.

586 In order to allow a meaningful comparison of modeled temperatures with temperatures measured in the  
587 boreholes, the uncertainty related to the timing of deglaciation at the specific borehole location resulting  
588 from the lateral ice retreat function (max. 2 years, cf. section 3.2) was corrected to get the true year of  
589 deglaciation in the models by running the model for maximum to more years. Consistent with the results  
590 shown on Fig. 9c, all the measured temperature profiles show an inverse temperature gradient at least in  
591 the upper part of the borehole, which reflects the preserved cold temperature from the glacial occupation at  
592 depth and a more recent warming trend.

593 Fig. 9d shows that the measured temperature profile of B2 is not exactly reproduced with our conduction  
594 model and the applied boundary conditions. However, the modelled shape of the profile and depth of the  
595 warming front is similar to that measured at this borehole location (Fig. 9d). The measured temperature  
596 profile is shifted by about 0.4° C to colder temperatures compared to the modeled values and has temper-  
597 atures of around 0° C at a depth of 20 to 25 m.

598 Annual mean temperatures measured in borehole B4 can be well reproduced by the conduction model (Fig.  
599 9e). Nevertheless, the model shows a slightly slower warming at a depth below the annual thermally active  
600 layer and the borehole end. The measured temperature profiles within the thermally active layer (i.e., the  
601 uppermost ~ 20 m) deviate from the model because temperatures at these depths are subject to annual  
602 temperature variability that can differ from the used MAGT in the model.

603 Conversely, the measured temperature profile of B6 cannot be reproduced with our thermal conduction  
 604 models. The measured temperature profile in this borehole shows a very different shape and quicker warm-  
 605 ing of the subsurface compared to the simulated ground warming after ice retreat by only heat conduction  
 606 (Fig. 9f). The warming front, evident by the turning point to a positive geothermal gradient, is below 50 m in  
 607 the measured temperature profile and significantly shallower in the results of the conduction model.



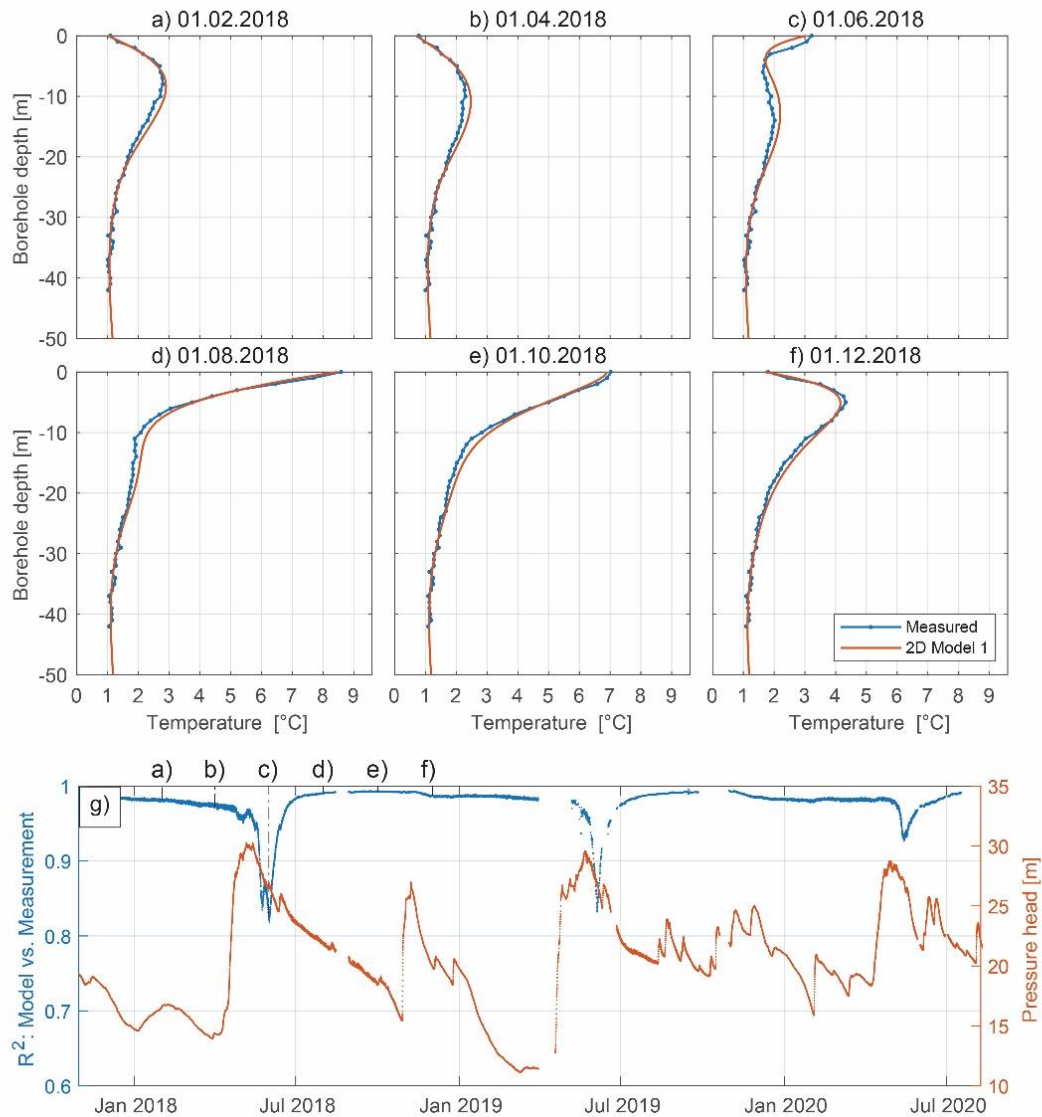
608

609 *Fig. 9. Results of the transient 2-D numerical model showing the annual mean subsurface temperature field for different*  
610 *ice elevations: (a) LIA ice extent; (b) 2019 ice extent. (c) Evolution of the annual mean subsurface temperature profile*  
611 *from 1860 to 2019 at the indicated mid-slope position c. Graphs d, e, and f show the comparison of the annual mean*  
612 *subsurface temperatures measured at the three borehole locations and the results from the 2-D numerical conduction*  
613 *model.*

#### 614 4.2.2. Seasonal temperature variations

615 As described above, the results from the annual mean subsurface temperature simulation show good agree-  
616 ment with the monitoring data in borehole B4 (section 4.2). Therefore, we investigated recent seasonal  
617 temperature variations (modeling step 3, section 3.2) at this location, and compared results to monitoring  
618 data. Fig. 10 shows a comparison of conduction-modeled and measured temperature profiles at different  
619 months during the year 2018. The results for other years are similar. The annual surface temperature vari-  
620 ability, both in the model and the monitoring data, affects a depth range of approximately 20 m. Measure-  
621 ments and model show a good accordance.

622 To investigate the mechanisms of seasonal temperature variations in detail, the correlation coefficient be-  
623 tween the modeled and measured temperature profile is calculated for each hourly time step and the R-  
624 squared value is plotted against time (see Fig. 10g). The small form letters in Fig. 10g indicate the timing of  
625 the different panels (Fig. 10a to f). The correlation coefficient time series shows a cyclic behavior with gen-  
626 erally very high values (above 0.95) from midsummer to winter. Lower correlation values are observed dur-  
627 ing spring and temporally correlate with strong pressure head rise in borehole B4, caused by snowmelt  
628 infiltration (see Fig. 10g). However, this negative peak in the R-squared value shows a delay compared to  
629 the pressure peak. Daily acquired photos from a time lapse camera installed at the opposite valley flank  
630 with view to the borehole locations show that this negative R-squared peak coincides with the time when  
631 the rock surface surrounding the borehole becomes snow free.



632

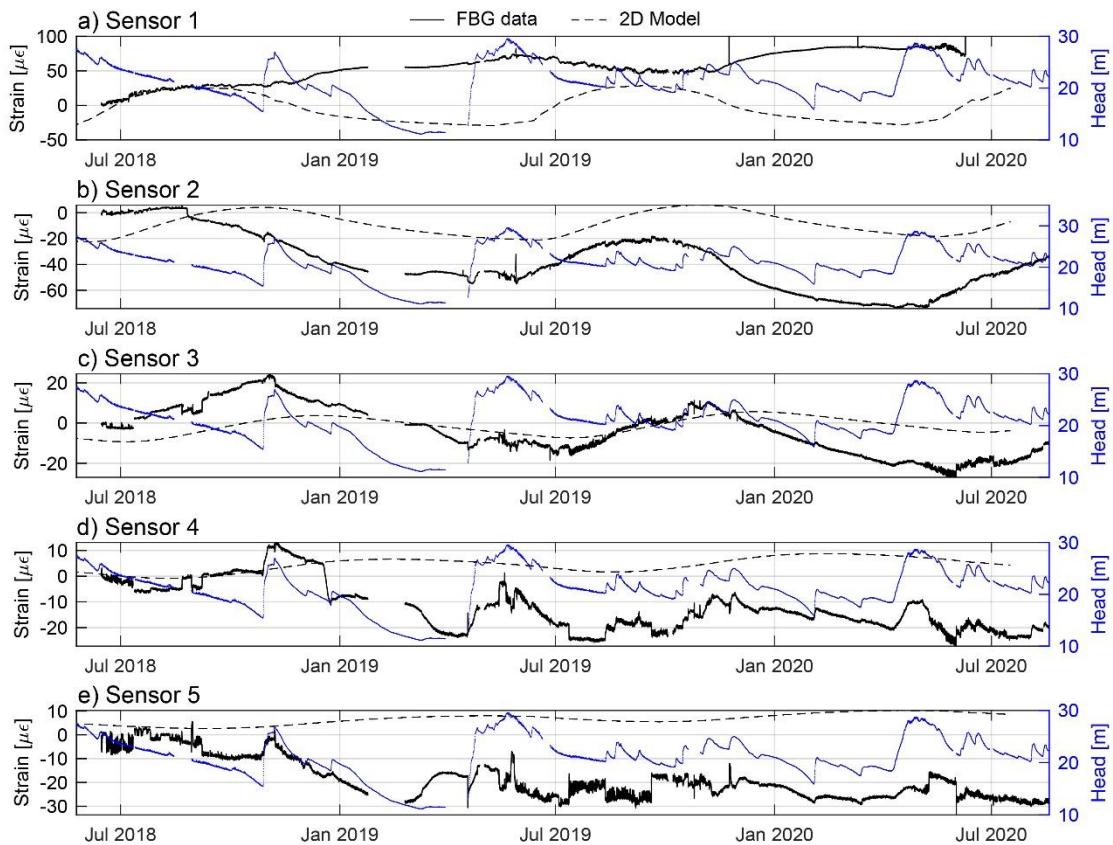
633 *Fig. 10. Panels a to f: Conduction-modeled temperature profiles together with the measured subsurface temperature*  
 634 *profile at borehole location B4 at specific time steps over the time span of 1 years. Panel g: Correlation (R-squared*  
 635 *value) between the measured subsurface temperatures in borehole B4 and the 2D heat conduction model results over*  
 636 *time. Additionally, the pressure head measured at the borehole end of B4 is provided. The small form letters indicate*  
 637 *the timing of the plots a to f.*

#### 638 4.2.3. Thermoelastic strain

639 Finally, we investigate the magnitude of thermoelastic strains in the subsurface resulting from seasonal  
 640 temperature cycles (Fig. 11). This is based on a comparison between monitored and modelled thermoelastic

641 strains in borehole B4 which is dominated by conductive heat transport. In addition, the pressure head  
642 measured at the borehole end is provided in the Fig. 11.

643 The numerical modeling shows that thermoelastic deformation occurs in the thermally active layer, and  
644 decreases with depth. The results show that the strain signal of the uppermost sensor cannot be reproduced  
645 by the simplified thermoelastic continuum model (Fig. 11a). However, strain readings of FBG-sensors num-  
646 ber 2 and 3 show a clear annual cyclicity with similar amplitude and phase as the modeled strain (Fig. 11b  
647 and c). In the strain signal of sensor 4 (Fig. 11d), a weak cyclic signal with an annual period and an ampli-  
648 tude similar to the modeled one might be superimposed to another signal strongly correlating with the local  
649 pressure head. In the deeper FBG-sensors, the modeled thermoelastic strain is an order of magnitude (or  
650 more) lower than the actual strain measured in the borehole. Further, the strain variations in these depths  
651 often coincide with pressure head fluctuations.



652

653 *Fig. 11. Comparison of the modeled thermo-elastic strain (dashed line), the measured strain in the borehole for the*  
654 *uppermost 5 FBG strain sensors (solid black line), and the pressure head (blue line) measured at the borehole end in*  
655 *borehole B4. Sensor depth intervals: 1: 0 – 4.3 m; 2: 4.3 – 8.6 m; 3: 8.6 – 12.9 m; 4: 12.9 – 17.2 m, 5: 17.2 – 21.5 m.*

## 656 5. Discussion and interpretation

### 657 5.1. Controls on subsurface temperature at a retreating glacier margin

658 Heat transfer by conduction through the rock mass is an important process explaining many observations  
659 of our shallow paraglacial temperature field. Measured temperatures in borehole B4 can be well reproduced  
660 with the 2-D heat conduction models and the results for B2 suggest that conduction plays an important role  
661 as well. Conversely, the temperature profile measured in borehole B6 strongly deviates from an expected  
662 conduction dominated regime and hence cannot be explained with this process. Additionally, all boreholes  
663 display a warming trend, which is likely caused by glacier retreat and subsequent exposure of the slope to  
664 annual temperature cycles. The propagation depth of this warming trend is observed to increase in depth  
665 the longer a borehole has been ice free.

666 Non-conductive heat transport processes at our monitoring boreholes are potentially driven by groundwater  
667 interaction with the adjacent glacier and yearly recharge cycles on the ice free slope. Typical patterns of  
668 such advective temperature disturbances have been discussed by Ge (1998) who distinguishes between  
669 (1) distributed vertical groundwater flow in semiconfined porous aquifers, (2) horizontal flow in confined  
670 aquifers, and (3) localized groundwater flow in preferential groundwater pathways such as fractures in  
671 gneiss and granite, all causing substantially different signatures (Bredehoeft and Papaopulos, 1965; Ge,  
672 1998). Such localized groundwater flow through fractures is assumed to be the cause for the observed  
673 positive and negative temperatures anomalies along the profiles (cf. Hugentobler et al., 2020). In order to  
674 develop localized thermal anomalies, the water flowing in transmissive fractures has to be in thermal dise-  
675 quilibrium with the surrounding rock and must be forced to flow by a natural head gradient, e.g. resulting  
676 from a stationary or transient groundwater flow field in an inclined slope.

677 In borehole B2, Fig. 9d shows a temperature offset of the modeled profile from the measured data of about  
678 0.4° C between depths of 25 m and 50 m. This deviation can be explained by cooling the subsurface with  
679 cold water directly connected to glacial ice, which could have caused temperatures of around 0° C down to

680 a borehole depth of 25 m during the time of ice occupation. We suggest that the high fracture density in this  
681 shallow layer (see Fig. 2) containing many open joints with confirmed high transmissivity from injection tests  
682 (cf. section 2.2), as well as the relatively low normal distance (~ 18 m at borehole meter 25) to the rock  
683 surface, enabled efficient advective heat transfer during time of ice occupation and during the years when  
684 the glacial ice was still close (i.e., 2018 and 2019). The measured temperature increase at around 25 m that  
685 is observed between 2019 and 2020 (Fig. 4d) can be related to a decoupling from the advective glacial  
686 hydraulic system due to the ongoing ice retreat and the penetration of the conductive warming front from  
687 the surface.

688 Relatively minor non-conductive heat transport processes are likely occurring at the B4 borehole location.  
689 This is evident when comparing the seasonal variability of the temperature profile measured in the borehole  
690 with the 1-D analytical solution and the 2-D numerical modeling results (Figs. 5 and 10). The correlation  
691 values reveal an annual repeating decrease during the time of snowmelt in spring, indicating a secondary  
692 heat transport process superimposed on the purely conductive transport model (Fig. 10g). Lower correla-  
693 tions are observed in the upper 20 to 30 m of borehole B4. The peak of the reduced correlation values  
694 occurs a few weeks after the pore pressure peak (recorded at 43.75 m depth), at a time when the borehole  
695 location becomes snow-free. We attribute the observed low correlation to advective heat transfer processes  
696 related to water infiltration happening directly at the borehole location.

697 Borehole B6 temperature measurements cannot be explained using a conduction model, the thermally ac-  
698 tive layer is 10 m deeper as compared to B2 and B4, and the measurements display larger temperature  
699 variations. This borehole is located within an inactive (presumably dormant) landslide body with substantially  
700 more disturbed and damaged rock mass compared to the other two borehole locations (cf. section 2). Ad-  
701 ditionally, a creek fed by nearby regional springs passes through a morphological depression next to the  
702 borehole. During drilling in fall 2017, bubbles from the pressurized air used for drilling extruded all around  
703 this depression, revealing a high transmissivity in the shallow subsurface. It is assumed that the availability  
704 of creek water to infiltrate into the subsurface at this location and higher transmissivity due to the disturbed  
705 rock mass enables strong advective heat transfer processes to occur in the shallow subsurface, as docu-  
706 mented in Anderson (2005).

## 707 5.2. Deformation and implications for rock mass weakening

### 708 5.2.1. Strains in the thermally active layer

709 The analyses of chapter 4.1.3 and 4.2.3 have revealed differences in the drivers of the FBG strain signals  
710 as a function of depth, as well as between the borehole locations. All boreholes feature an annual cyclic  
711 strain signal in shallow sensors that shows accordance with ground temperature and a slight phase shift  
712 with depth. Given the correlation to ground temperature, as well as the results of the numerical modeling  
713 (Fig. 11), it is likely that this component corresponds to thermoelastic deformation.

714 This can be clearly demonstrated in our monitoring data of borehole B4 with the most intact rock mass  
715 conditions. The FBG data from sensor 2 and 3 (Fig. 11), which correspond to depth intervals of 4.6 to 8.9  
716 m and 8.9 to 13.2 m, show that here the cyclic, thermoelastic deformation signal dominates over other  
717 signals. Deeper in the borehole (i.e., from ~ 13.2 m downwards) other signals, that show minor or no corre-  
718 lation with the modeled thermoelastic deformation, dominate the strain time series. In borehole B2 and B6,  
719 with less intact rock mass conditions, the uppermost few sensors also show signals with an annual cyclicity  
720 that is attributed to thermoelastic effects. However, this continuous cyclic deformation is interrupted by ab-  
721 rupt strain events of similar magnitude or superimposed by sometimes even stronger deformation trends  
722 (e.g., label a in Fig. A 3). Additionally, most shallow sensors in all three boreholes show a long term negative  
723 strain trend.

724 An exception is the strain signal measured in the uppermost sensor of all boreholes, which shows an inverse  
725 correlation with the model data and hence must be related to a different driving mechanism. Expansion in  
726 wintertime and contraction in summertime could be caused by the effect of hygroscopic expansion or mois-  
727 ture induced strain (e.g., Gor et al., 2017) and related to potentially higher relative humidity in the shallow  
728 rock layer below the snowpack compared to dry summer conditions. Another possibility to generate exten-  
729 sional strain in wintertime and contraction in summer are frost weathering processes such as volumetric  
730 expansion or ice segregation (Draebing et al., 2017). However, this is unlikely to be the reason for the  
731 measured strain at the uppermost sensor as no negative subsurface temperatures were measured in win-  
732 tertime.

### 733 5.2.2. Strains below the thermally active layer

734 Some multi-annual strain time-series measured in deeper sensors clearly correlate with pressure head rec-  
735 ords in the corresponding borehole (e.g., sensor 4 and 5 in Fig. 11) and hence are probably strongly driven  
736 by poroelastic hydromechanical effects. Other sensors show rapid or short-term strain events often tempo-  
737 rally coinciding with pressure head changes or precipitation events but overall show a low correlation to the  
738 pressure head time-history (e.g., FBG-9, 10 in B4, Fig. A 2). We explain this diversity of reactions with the  
739 complex nature of hydromechanical drivers and coupled deformations in our fractured rock slope. The re-  
740 sponse of an individual FBG monitoring interval to a pressure perturbation strongly depends on the local  
741 stress conditions, and the number, orientation and type of fractures intersected by the interval (Krietsch et  
742 al., 2020).

743 In a paraglacial setting the impact of the adjacent glacier on deformations recorded in the slope can be  
744 manyfold and are presented in a companion paper. Effective glacial ice load changes, due to variations in  
745 the subglacial water pressures related to daily meltwater cycles and rainfall infiltration into the glacier during  
746 summertime, might be strong enough to cause measurable strain, pore pressure cycles and additional hy-  
747 dromechanically coupled effects. Also, the higher relative number of strain events detected in deeper, pore  
748 pressure controlled sensors compared to the sensors within the thermally active layer (evident in the cumu-  
749 lative sum plots of Fig. 7), can be related to hydromechanical effects. During summer and fall a higher  
750 activity in the hydraulic systems of the slope and glacier must be expected, i.e. groundwater recharge by  
751 snowmelt and rainfall infiltration induce recharge variations and higher hydraulic gradients in the rock slope,  
752 and daily ice melt in summer strongly increases the dynamics of the subglacial hydrological system (Harper  
753 et al., 2005). We interpret these effects to be the reason for the observed increased number of strain events  
754 occurring during the summer season.

### 755 5.2.3. Irreversible rock mass damage

756 As discussed in the previous section, strain signals during our 2.5-year monitoring period are partly driven  
757 by thermomechanical and hydromechanical processes. The majority of our detected short-term and rapid  
758 strain events coincide with precipitation events, of which about 50 % were strong enough to cause a clear  
759 reaction in the pore pressure signal at 40-50 m depth.

760 To identify rock mass damage, reversible (elastic) strains and irreversible (plastic) strains have to be distin-  
761 guished (cf. Hugentobler et al., 2020), and the drivers for the specific strain signals need to be investigated.  
762 A strain signal is interpreted as reversible if it returns to its initial value after a given stress perturbation. In  
763 contrast, irreversible strain is the offset that remains after a stress perturbation. However, for longer-term  
764 drivers of deformation, such as unloading due to glacial retreat, which is probably a continuously ongoing  
765 process at the time scale of our monitoring period, this distinction is not possible. In that case we use strain  
766 characteristics (e.g., orientation, spatial differences in strain signals) and additional data such as disconti-  
767 nuity occurrence and orientation to discuss if the signal may be reversible or irreversible. Based on these  
768 definitions rock mass damage could either involve fracture slip, controlled by friction and fracture of asperi-  
769 ties, or fracture propagation, controlled by stress intensity and stress corrosion. The available monitoring  
770 data can not clearly distinguish the two processes, but considering the size of the mapped fractures, we  
771 assume that slip is the dominant process observed.

772 Hence, most rapid events (e.g., label b in Fig. A 2) are interpreted as irreversible fracture slip or fracture  
773 propagation driven by pore pressure fluctuations or presumably also glacial load changes from varying en-  
774 glacial water levels. Short-term strain events often show similarities to pressure head signals (e.g., label a  
775 in Fig. A 2) with a strongly reversible strain component and a minor irreversible component. We relate the  
776 reversible portion of these strain events to poroelastic reactions and the often present minor irreversible  
777 component to plastic deformation and progressive rock mass damage. Therefore, many of the automatically  
778 detected rapid and short-term strain events contain at least a minor irreversible strain component, which  
779 means that the irreversible deformation is also strongly controlled by hydromechanical effects. This obser-  
780 vation agrees with the numerical modeling results of Grämiger et al. (2020), who concluded that hydrome-  
781 chanical effects are more effective in generating long term damage in paraglacial rock slopes compared to  
782 thermomechanical effects.

783 The strain time series also contain 20 to 30 % short-term strain events that cannot directly be related to any  
784 of the investigated drivers. We suggest that these signals may be related to fatigue processes occurring in  
785 the studied rock slope. As summarized in the introduction, cyclic stresses can promote rock fatigue and

786 drive fracture propagation. In our studied slopes, cyclic loading is mainly driven by annual temperature var-  
787 iations, daily and annual pore pressure fluctuations and presumably also daily fluctuations of the mechanical  
788 load placed on the slope by the Aletsch glacier. In the shallow subsurface, cyclic thermal loading from annual  
789 temperature variations dominates the reversible signal causing largest strain amplitudes of  $\sim 60 \mu\epsilon$  within  
790 the uppermost 4 m and strain amplitudes decreasing with depth to  $\sim 5 \mu\epsilon$  at around 20 m depth. Below  
791 around 12 m depth, reversible strain cycles show amplitudes of up to  $\sim 20 \mu\epsilon$ , are driven by pressure head  
792 fluctuations due to snowmelt infiltration or heavy rainfalls and normally occur at frequencies greater than  
793 1/yr. The fact that these strain events often comprise a minor irreversible strain component, shows that  
794 many fractures may be close to a critical stress state. This could imply that fractures in our slope normally  
795 deform or grow slowly under subcritical conditions supported by cyclic fatigue, but that stronger loading  
796 events trigger critical crack slip or propagation.

797 The overall negative strain observed in many sensors of all boreholes is composed of (1) a slow, continuous  
798 long-term strain signal that can be observed in several sensors (Fig. A 1, A 2, and A 3, Appendix) and (2)  
799 the accumulation of deformation from the short-term strain events discussed above. Because of the limited  
800 time of monitoring, it is not clear if these longer-term strain trends reflect reversible (elastic) or irreversible  
801 (plastic) deformation. Elastic deformation in such deglaciating rock slopes could be caused by rock mass  
802 extension due to unloading from ice downwasting or thermal expansion related to the observed ground  
803 warming after ice retreat. However, these perturbations would cause an extension of the rock mass, which  
804 is the opposite of what we observe in our monitoring data. On the other hand, compressive strain can orig-  
805 inate either from slip along toppling fractures steeply dipping into the slope or from slip along sliding fractures  
806 dipping in downslope direction (cf. Fig. 15 in Hugentobler et al., 2020). Fractures of both orientations fre-  
807 quently occur at our study site (Hugentobler et al., 2020). We therefore interpret these negative strain trends  
808 to be irreversible and related to progressive rock mass damage in our deglaciating rock slope.

809 We find that the magnitude of measured strain responses depends on the local rock mass quality at the  
810 given borehole location. This is observed in our research boreholes, as strong pore pressure variations  
811 (e.g., due to the heavy rainstorm in early Oct. 2020) cause minor irreversible responses in the more intact  
812 rock mass of B4 (Fig. A 2), but very clear irreversible deformation in the more strongly disturbed rock mass

813 around B2 (label b in Fig. A 1). This observation is consistent with the numerical investigations of Gischig  
814 et al. (2011a) and Grämiger et al. (2020), who show that the efficiency of thermomechanical and hydrome-  
815 chanical loading cycles for fracture propagation (damage) in fractured crystalline rocks strongly depend on  
816 the magnitude of the drivers, as well as the initial damage state or criticality of the rock mass.

### 817 5.3. Implications for paraglacial rock slope evolution

818 Our measurements indicate that a significant portion of paraglacial strains occur in the uppermost 50 meters.  
819 This is confirmed by a comparison of horizontal ground surface displacements with integrated horizontal  
820 borehole strains from the SAA inclinometer chain at borehole B4 (Hugentobler et al. 2020).

821 If our interpretations of the underlying mechanisms hold, near-surface hygroscopic expansion can induce  
822 reversible annual strains, which are even larger than the thermo-elastic and poroelastic slope deformations  
823 occurring at greater depth. The magnitude of annual vertical strain (50 - 100  $\mu\epsilon$ ) induced by variations in  
824 moisture content is at the lower end of what has been derived from lab tests on intact and fractured granite  
825 with humidity increase from 20% to 80% (Li et al., 2021). Annual thermoelastic strain magnitudes of about  
826 20 - 50  $\mu\epsilon$  at 5 - 10 m depth are consistent with continuum modeling results and an in-situ derived thermal  
827 diffusivity. Annual poroelastic strain cycles are less clearly defined in our borehole pressure records, mainly  
828 due to the complex interactions of englacial and slope hydrologic systems.

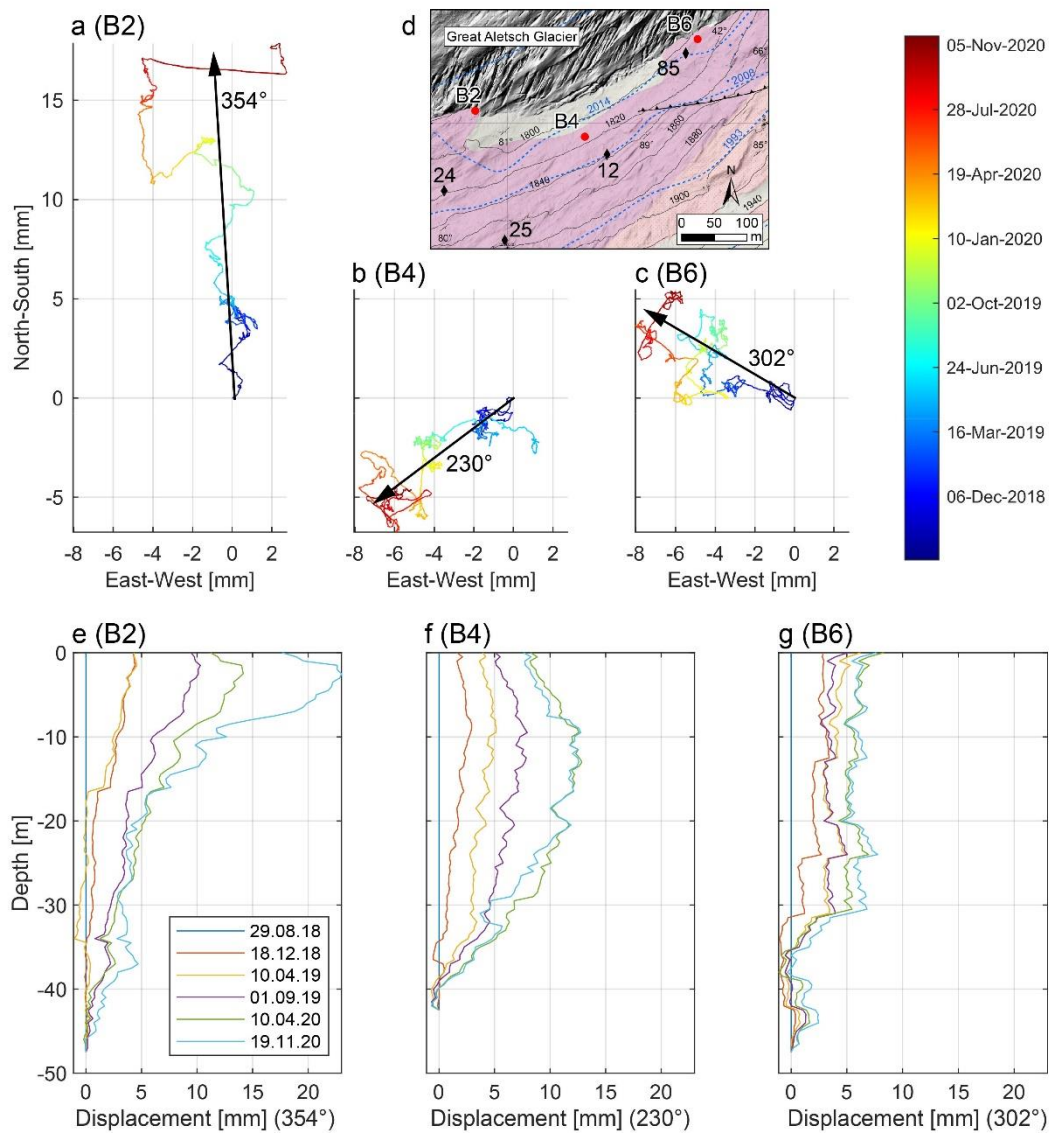
829 Modeled and measured longer-term subsurface temperature changes related to the ground warming effect  
830 after ice retreat could not be related to monitored strain at our depth of investigation. We explain this with  
831 the low expected strain magnitudes resulting from the minor temperature changes of below 1° C in three  
832 years, but also to the occurrence of other drivers such as pore pressure or presumably glacial load changes  
833 that cause stronger superimposed strain reactions dominating the signal below the thermally active layer.  
834 Hence, our findings agree with previous work that showed that thermomechanical effects contribute to pro-  
835 gressive rock mass damage in deglaciating environments (Baroni et al., 2014; Grämiger et al., 2018), but  
836 that the longer-term effects are minor compared to the stronger hydromechanical and mechanical drivers  
837 that occur at greater frequencies during rock slope deglaciation.

838 As visible in our pore pressure data (borehole B4 vs. B6), local hydraulic properties of the rock mass control

839 the magnitude of pore pressure fluctuations and therefore the relative importance of hydromechanical ver-  
840 sus thermomechanical driven strain at a specific location within the slope. Our study only includes observa-  
841 tions close to a retreating glacier margin. In fractured rock slopes the depth of the groundwater water table  
842 below surface generally increases towards the crest. In the upper left (southern) slope of the Aletsch Valley,  
843 the groundwater table elevation is expected to occur at several 100 meters depth (Grämiger et al., 2020).  
844 Therefore, the relative importance of thermomechanical loading effects might increase with greater distance  
845 to the ice margin.

846 Our monitoring data shows that numerous rapid and presumably also slow slip events along steeply and  
847 moderately dipping fractures (Fig. 2) are superimposed on long-term seasonal strains and multi-annual  
848 strain trends. Cumulative slip reaches similar or higher displacement magnitudes than the elastic defor-  
849 mations reported above. Most of these slip events are irreversible and small ( $< 20 \mu\epsilon$ ) and the total displace-  
850 ment can locally be controlled by a few rare events, such as the 80 mm rainstorm of October 2020 (label b  
851 in Fig. A 1). All these events contribute to very slow irreversible slope movements, even in slopes considered  
852 stable. Cumulative displacement magnitudes of these movements as derived from the (horizontal) inclinom-  
853 eter readings range from 8 to 17 mm in two years (see Fig. 12), and 2 to 10 mm for vertical irreversible  
854 deformation along our 50 m deep boreholes. Such creep rates are high compared to the irreversible hori-  
855 zontal slope displacements modeled by Grämiger et al. (2020) for a full glacial cycle. In their modeling  
856 results, highest displacements occur close to the slope toe (at the location of our monitoring boreholes), but  
857 only reach 25 cm after 500 annual cycles. One reason for the lower displacement rates in their numerical  
858 models could be related to the simplified assumptions regarding hydraulic and mechanical boundary condi-  
859 tions (especially at sub-annual timescales) and the neglect of subcritical fracture propagation mecha-  
860 nisms. On the other hand, our observed irreversible strain rates cannot occur permanently over thousands  
861 of years at the whole slope because this would cause unrealistic high overall slope deformations. This could  
862 imply that – as previously suggested – strongest cyclic loading, fatigue and damage occurs directly at the  
863 glacier margin and decays with lateral upslope distance. This might also explain the surprisingly high frac-  
864 ture apertures and borehole transmissivities recorded at the borehole locations, in a slope generally showing  
865 strong rock with high rock mass quality.

866 Following this hypothesis, long-term rock slope damage might be driven by accumulated damage occurring  
867 at the glacier margin during multiple glacial cycles. In the Great Aletsch Glacier valley the Holocene mini-  
868 mum is located very close (downstream) of our borehole locations (Fig. 1). This implies that many Holocene  
869 glacier advance and retreat cycles occurred above our research borehole locations, and especially in the  
870 valley below the Holocene minimum (cf. Grämiger et al., 2017). This matches very well with the mapped  
871 landslide distribution in the Aletsch valley, showing a clear landslide density hotspot below the Holocene  
872 minimum. And finally, also the few available ages of landslide initiation in this hotspot area (Glueer et al.,  
873 2020; Grämiger et al., 2017), match very well with this model of paraglacial damage mechanisms during  
874 multiple Holocene glacier retreat and advance cycles.



875

876 *Fig. 12: a, b, c: Map view illustrations of cumulative horizontal deformation over time of boreholes B2, B4, and B6*  
 877 *measured with the SAA in-place inclinometer system. The black arrows indicate the mean movement direction. d: Map*  
 878 *view of the three borehole locations. e, f, g: Cumulative displacements of each segment from the borehole end up to*  
 879 *the surface in direction of the main movement.*

## 880 6. Summary and conclusion

881 We use three full years of hourly measured borehole temperature and high resolution FBG strain monitoring  
 882 data to investigate the transient subsurface temperature regime and micrometer-scale deformation in a rock  
 883 slope adjacent to a retreating, temperate valley glacier. The presented data give unique new insights into

884 the thermomechanical and hydromechanical drivers of rock slope deformation adjacent to retreating glaciers  
885 over the monitored time scales. Detailed analysis of the subsurface deformation signals allow to identify  
886 various potential drivers for reversible (elastic) and irreversible deformation. This knowledge is important for  
887 understanding the main processes contributing to short- and long-term progressive rock mass damage that  
888 potentially lead to the formation of paraglacial rock slope instabilities. The most important findings of the  
889 present work can be summarized as follows:

- 890 1. The thermal investigation reveals that the subsurface temperatures at our monitored slope are cur-  
891 rently in a transient state adjusting to new surface temperature conditions after glacial ice retreat.  
892 We show that heat conduction is a dominant process and explains most of the observed transient  
893 subsurface temperatures at sites with intact rock, but locally strong deviations from a conduction  
894 dominated regime can occur. These deviations can be explained by nonconductive processes (e.g.,  
895 heat transfer by water) that become important when the rock mass is fractured (i.e., has an in-  
896 creased transmissivity), and are efficient when water and a hydraulic head gradient is available.  
897 The observed nonconductive temperature deviations in our study area are related to groundwater  
898 exchange with cold subglacial water, snowmelt infiltration, or creek water infiltration.
- 899 2. Our strain monitoring data analysis shows that annual surface temperature changes, precipitation  
900 events and pore pressure fluctuations are important drivers for deformation at our study site. How-  
901 ever, longer-term trends in the strain time series and a minority of short-term strain events cannot  
902 directly be related to any of the investigated drivers. We find that thermo-elastic effects due to an-  
903 nual temperature cycles dominate the strain signal in the uppermost 12 m of our stable fractured  
904 crystalline rock slope. Below this depth the hydromechanical effects dominate the deformation. Fur-  
905 ther, we show that both reversible and irreversible short-term deformation more frequently occur  
906 during summertime when the hydrological system in the rock slope and in the temperate glacier are  
907 more dynamic.
- 908 3. Irreversible deformation in our time series, which we relate with progressive rock mass damage,  
909 occurs as short-term or rapid strain events within hours or days and as slower, continuous strain  
910 trends (mainly in vertical contraction direction). We show that the majority of short-term strain events

911 coincide with precipitation events or pore pressure changes. Other potential drivers such as extreme  
912 surface temperatures or earthquakes occurring in the area do not show temporal correlation with  
913 strain events. We propose that cyclic fatigue from thermomechanical and hydromechanical loading  
914 cycles, can support long-term subcritical crack growth and micrometer-scale slope deformations  
915 even in presumably stable slopes.

916 4. We show that the magnitude of irreversible deformation depends on the magnitude of the driver but  
917 also on the spatially variable pre-existing damage at our three borehole locations. At our most stable  
918 borehole location, single events with irreversible strain magnitudes are normally on the order of a  
919 few  $\mu\epsilon$ , whereas at the more damaged borehole location irreversible strain magnitudes up to tens  
920 or few hundreds of  $\mu\epsilon$  have been recorded.

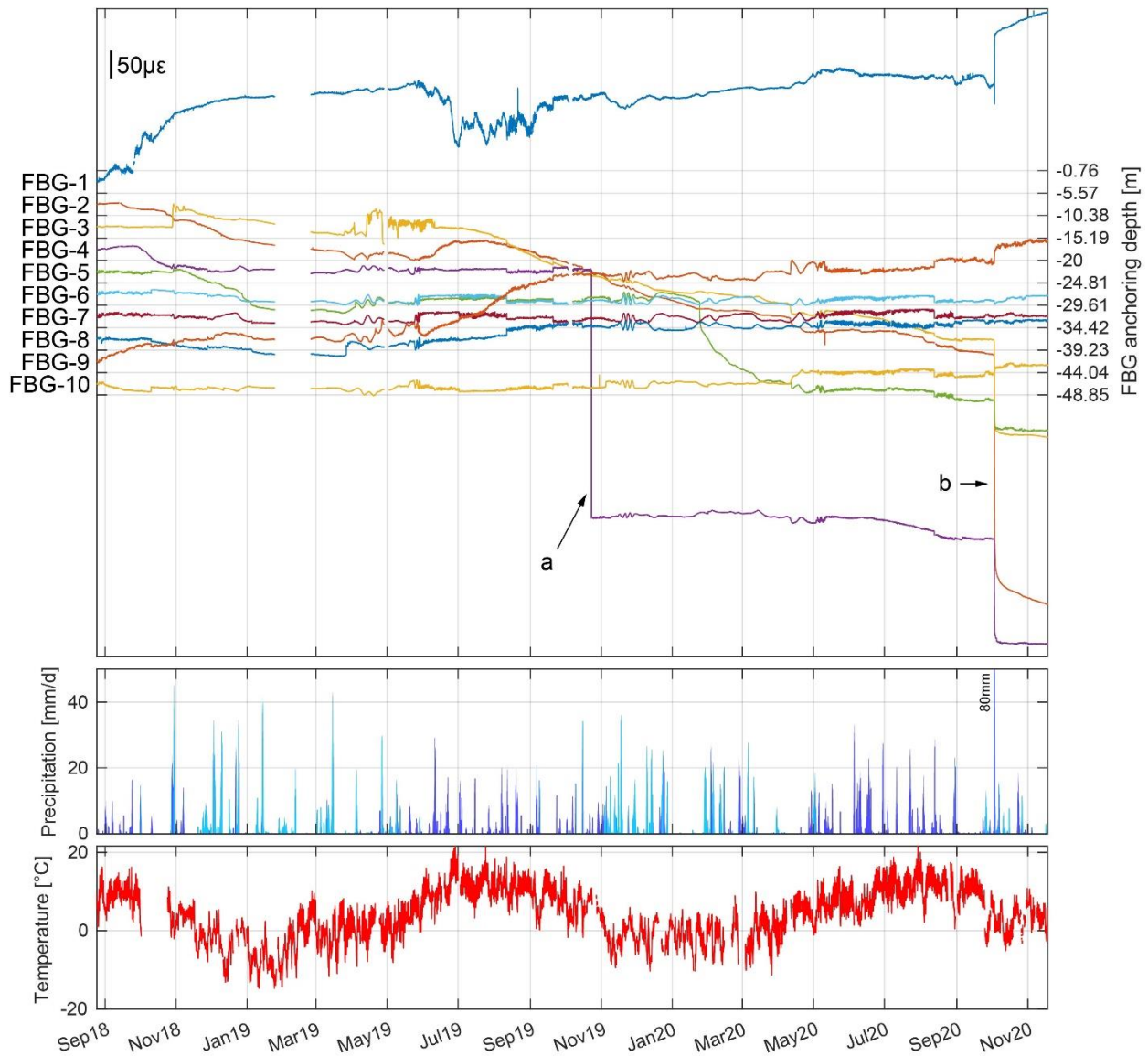
921 5. Our study shows that the complex strain signals in deglaciating rock slopes are driven by superim-  
922 posed thermo-hydro-mechanical effects, with relative magnitudes that vary over space and time  
923 (relative to ice retreat) controlled by factors such as rock mass properties, distance to the glacial  
924 margin, or depth. We propose that strongest cyclic loading, fatigue, and damage processes occur  
925 close to the glacier margin and decay with lateral upslope distance. Following this hypothesis, long-  
926 term damage accumulation close to the moving glacier margin during multiple glacial cycles could  
927 significantly contribute to the formation of paraglacial rock slope instabilities.

## 928 Acknowledgements

929 This project is funded by the Swiss National Science Foundation (project 172492). We want to thank Lukas  
930 Frei for his contributions in the framework of his bachelor thesis and Nicolas Oestreicher for sharing time-  
931 lapse images from the study site to constrain the timing of snow coverage at the borehole locations. Further,  
932 we thank Andrea Manconi for providing us seismic data and expert support to confirm the occurrence of  
933 precipitation events at the study site. Also, we want to thank Reto Seifert and the numerous field helpers  
934 who joined our maintenance visits and helped to keep the monitoring system running. Data is accessible  
935 under: <https://doi.org/10.3929/ethz-b-000505871>.

## 936 Appendix A: FBG strain monitoring data

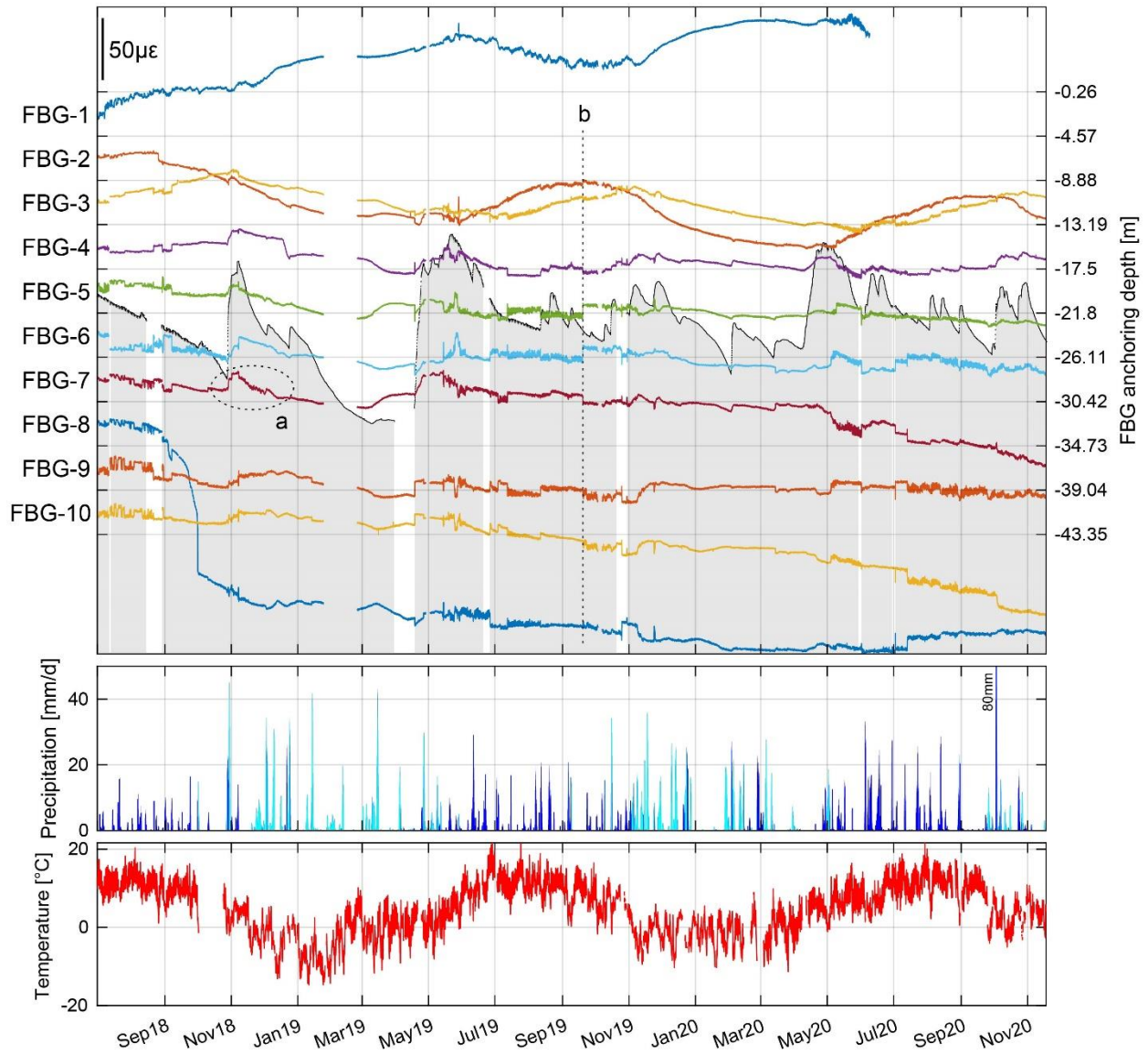
937 Fig. A 1, A 2, and A 3 contain the temperature corrected hourly mean FBG-strain measurements for each  
938 sensor in the three vertical research boreholes. The setup and detailed description of the monitoring system  
939 is provided in Hugentobler et al. (2020). All FBG sensors of the three boreholes contain a data gap of about  
940 one month in January 2019 which is related to a winter storm that broke the solar panel used for the power  
941 supply of the system. A second data gab of around two month duration is existing in FBG monitoring data  
942 of all sensors in borehole B6 in summer 2019 (Fig. A 3). This gap is related to the breakage of the reenforced  
943 fiber optical cable connecting the borehole location to the FBG data acquisition system that happened during  
944 a debris flow event. Furthermore, sensor 1 of boreholes B4 and B6 contain incomplete data recordings  
945 because of malfunctioning FBG temperature sensors causing traveling reflection peaks that sometimes in-  
946 terfere with the reflected light peaks from the strain sensors because of similar wavelength.



947

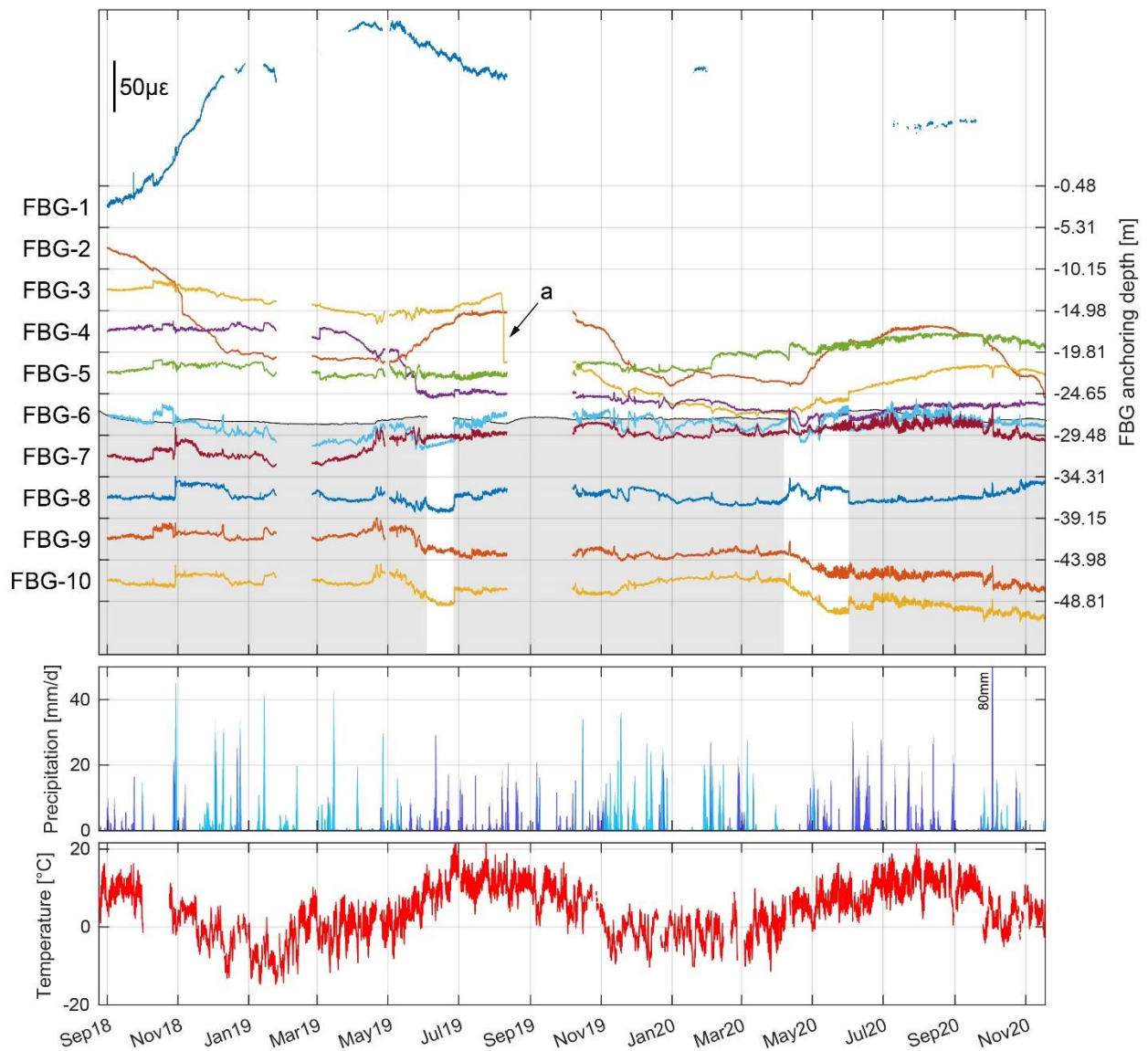
948 *Fig. A 1. Upper plot: The colored lines show a visualization of the temperature corrected strain data of the individual*  
 949 *4.81 m base-length FBG sensors installed in borehole B2. The strain data of each sensor is plotted in the center of the*  
 950 *specific depth interval, and the vertical axis ticks correspond to anchoring depth of the FBG sensors. Positive strain*  
 951 *means elongation and negative strain compaction of the sensor, and the strain scale is provided on the top left in*  
 952 *microstrain ( $\mu\epsilon$ ). Label a indicates a strain step in FBG-4 that was identified as a measurement artifact and corrected*  
 953 *before the analysis. Label b indicates a significant rapid strain event that was measured in many sensors, coincides*  
 954 *with an extreme rainfall event, and is referred to in the text. Lower plots: The vertical blue and cyan bars show the*  
 955 *cumulative total precipitation data (per 24 hours) provided by MeteoSchweiz from the weather station "Bruchji" (Valais)*  
 956 *located approximately 6 km away from our study site. The cyan colored bars indicate precipitation that presumably*

957 occurred as snow (i.e., at surface temperatures below 1°C at our study site (cf. Jennings et al., 2018)). Red time series  
 958 show surface temperatures measured at the study site during the monitoring period.



959  
 960 Fig. A 2. Upper plot: The colored lines show a visualization of the temperature corrected strain data of the individual  
 961 4.31 m base-length FBG sensors installed in borehole B4. The strain data of each sensor is plotted in the center of the  
 962 specific depth interval, and the vertical axis ticks correspond to anchoring depth of the FBG sensors. Positive strain  
 963 means elongation and negative strain compaction of the sensor, and the strain scale is provided on the top left in  
 964 microstrain ( $\mu\epsilon$ ). Additionally, the elevation of the pressure head in the borehole is provided as a gray area in the back-  
 965 ground of the plot. Labels a and b indicate strain events referred to in the text. Lower plots: The vertical blue and cyan

966 bars show the cumulative total precipitation data (per 24 hours) provided by MeteoSchweiz from the weather station  
 967 "Bruchji" (Valais) located approximately 6 km away from our study site. The cyan colored bars indicate precipitation that  
 968 presumably occurred as snow (i.e., at surface temperatures below 1°C at our study site (cf. Jennings et al., 2018)). Red  
 969 time series show surface temperatures measured at the study site during the monitoring period.



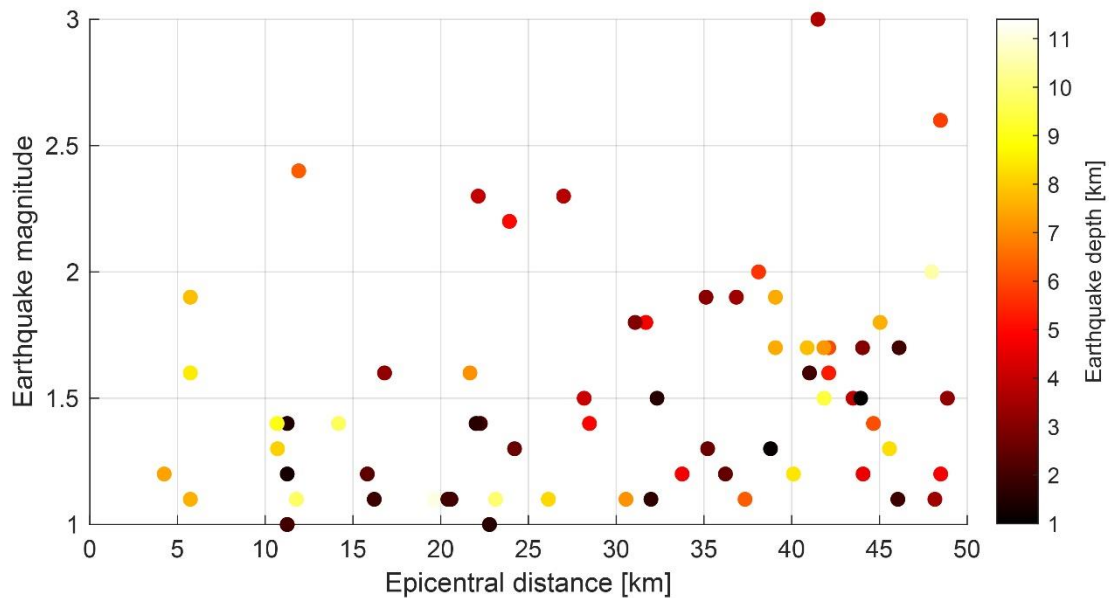
970  
 971 Fig. A 3. Upper plot: The colored lines show a visualization of the temperature corrected strain data of the individual  
 972 4.83 m base-length FBG sensors installed in borehole B6. The strain data of each sensor is plotted in the center of the  
 973 specific depth interval, and the vertical axis ticks correspond to anchoring depth of the FBG sensors. Positive strain  
 974 means elongation and negative strain compaction of the sensor, and the strain scale is provided on the top left in

975 microstrain ( $\mu\epsilon$ ). Additionally, the elevation of the pressure head in the borehole is provided as a gray area in the back-  
976 ground of the plot. Label a indicates a strain event referred to in the text. Lower plots: The vertical blue and cyan bars  
977 show the cumulative total precipitation data (per 24 hours) provided by MeteoSchweiz from the weather station "Bruchji"  
978 (Valais) located approximately 6 km away from our study site. The cyan colored bars indicate precipitation that presum-  
979 ably occurred as snow (i.e., at surface temperatures below 1°C at our study site (cf. Jennings et al., 2018)). Red time  
980 series show surface temperatures measured at the study site during the monitoring period.

## 981 Appendix B: Earthquake events

982 In Fig. B 1 all earthquake events used for the comparison with the strain events measured in our research  
983 boreholes are characterized by means of earthquake magnitude, epicentral distance to the study site, and  
984 earthquake depth. We used all recorded earthquakes that occurred during our monitoring period with mag-  
985 nitudes greater than M1, epicentral distances of less than 50 km to our study site, and with depth between  
986 0 and 15 km.

987



988

989 Fig. B 1. Earthquake catalog used for the comparison with strain events detected in our research boreholes (data pro-  
990 vided by the Swiss Seismological Service (SED)). The earthquake magnitude is provided vs. the epicentral distance of

991 the individual earthquake event from our study site. Depths information for the individual earthquake events are shown  
992 with the color scale.

## 993 7. References

- 994 Anderson, M. P. (2005), Heat as a ground water tracer, *Ground Water*, 43(6), 951-968,  
995 doi:10.1111/j.1745-6584.2005.00052.x.
- 996 Attewell, P. B., and I. W. Farmer (1973), Fatigue behaviour of rock, *International Journal of Rock*  
997 *Mechanics and Mining Sciences & Geomechanics Abstracts*, 10(1), 1-9, doi:10.1016/0148-  
998 9062(73)90055-7.
- 999 Ballantyne, C. K., G. F. Sandeman, J. O. Stone, and P. Wilson (2014), Rock-slope failure following  
1000 Late Pleistocene deglaciation on tectonically stable mountainous terrain, *Quaternary Science*  
1001 *Reviews*, 86, 144-157, doi:10.1016/j.quascirev.2013.12.021.
- 1002 Baroni, C., S. Martino, M. C. Salvatore, G. S. Mugnozza, and L. Schiliro (2014), Thermomechanical  
1003 stress-strain numerical modelling of deglaciation since the Last Glacial Maximum in the Adamello  
1004 Group (Rhaetian Alps, Italy), *Geomorphology*, 226, 278-299,  
1005 doi:10.1016/j.geomorph.2014.08.013.
- 1006 Bodri, L., and V. Čermák (1995), Climate changes of the last millennium inferred from borehole  
1007 temperatures: Results from the Czech Republic—Part I, *Global Planet Change*, 11(3), 111-125,  
1008 doi:10.1016/0921-8181(95)00005-4.
- 1009 Bodri, L., and V. Čermák (1999), Climate change of the last millennium inferred from borehole  
1010 temperatures: regional patterns of climatic changes in the Czech Republic — Part III, *Global Planet*  
1011 *Change*, 21(4), 225-235, doi:10.1016/S0921-8181(99)00044-2.
- 1012 Brain, M. J., N. J. Rosser, E. C. Norman, and D. N. Petley (2014), Are microseismic ground  
1013 displacements a significant geomorphic agent?, *Geomorphology*, 207, 161-173,  
1014 doi:10.1016/j.geomorph.2013.11.002.
- 1015 Bredehoeft, J. D., and I. S. Papaopulos (1965), Rates of vertical groundwater movement estimated  
1016 from the Earth's thermal profile, *Water Resources Research*, 1(2), 325-328,  
1017 doi:10.1029/WR001i002p00325.
- 1018 Brown, E. T., and J. A. Hudson (1973), Fatigue failure characteristics of some models of jointed rock,  
1019 *Earthquake Engineering & Structural Dynamics*, 2(4), 379-386, doi:10.1002/eqe.4290020407.
- 1020 Cerfontaine, B., and F. Collin (2018), Cyclic and Fatigue Behaviour of Rock Materials: Review,  
1021 Interpretation and Research Perspectives, *Rock Mech Rock Eng*, 51(2), 391-414,  
1022 doi:10.1007/s00603-017-1337-5.
- 1023 Choi, S.-J., K. G. Park, C. Park, and C. Lee (2021), Protection and Installation of FBG Strain Sensor  
1024 in Deep Boreholes for Subsurface Faults Behavior Monitoring, *Sensors*, 21(15),  
1025 doi:10.3390/s21155170.
- 1026 Deprez, M., T. De Kock, G. De Schutter, and V. Cnudde (2020), A review on freeze-thaw action and  
1027 weathering of rocks, *Earth-Sci Rev*, 203, 103143, doi:10.1016/j.earscirev.2020.103143.
- 1028 Draebing, D., and M. Krautblatter (2019), The efficacy of frost weathering processes in alpine  
1029 rockwalls, *Geophys Res Lett*, 46(12), 6516-6524, doi:10.1029/2019GL081981.
- 1030 Draebing, D., M. Krautblatter, and T. Hoffmann (2017), Thermo-cryogenic controls of fracture  
1031 kinematics in permafrost rockwalls, *Geophys Res Lett*, 44(8), 3535-3544,  
1032 doi:10.1002/2016gl072050.

- 1033 Eppes, M. C., and R. Keanini (2017), Mechanical weathering and rock erosion by climate-dependent  
1034 subcritical cracking, in *Rev. Geophys.*, edited, pp. 470-508, doi:10.1002/2017RG000557.
- 1035 Ge, S. (1998), Estimation of groundwater velocity in localized fracture zones from well temperature  
1036 profiles, *Journal of Volcanology and Geothermal Research*, 84(1), 93-101, doi:10.1016/S0377-  
1037 0273(98)00032-8.
- 1038 Gischig, V., G. Preisig, and E. Eberhardt (2016), Numerical Investigation of Seismically Induced Rock  
1039 Mass Fatigue as a Mechanism Contributing to the Progressive Failure of Deep-Seated Landslides,  
1040 *Rock Mech Rock Eng*, 49(6), 2457-2478, doi:10.1007/s00603-015-0821-z.
- 1041 Gischig, V. S., J. R. Moore, K. F. Evans, F. Amann, and S. Loew (2011a), Thermomechanical forcing  
1042 of deep rock slope deformation: 1. Conceptual study of a simplified slope, *J Geophys Res-Earth*,  
1043 116, doi:10.1029/2011jf002006.
- 1044 Gischig, V. S., J. R. Moore, K. F. Evans, F. Amann, and S. Loew (2011b), Thermomechanical forcing  
1045 of deep rock slope deformation: 2. The Randa rock slope instability, *J Geophys Res-Earth*, 116,  
1046 doi:10.1029/2011jf002007.
- 1047 GLAMOS (1881-2019), The Swiss Glaciers 1880-2016/17, Glaciological Reports No 1-138,  
1048 Yearbooks of the Cryospheric Commission of the Swiss Academy of Sciences (SCNAT),  
1049 published since 1964 by VAW / ETH ZurichRep.
- 1050 GlaThiDa\_Consortium (2019), Glacier Thickness Database 3.0.1., edited by W. G. M. Service,  
1051 Zurich, Switzerland, doi:10.5904/wgms-glathida-2019-03.
- 1052 Glueer, F., S. Loew, and A. Manconi (2020), Paraglacial history and structure of the Moosfluh  
1053 Landslide (1850–2016), Switzerland, *Geomorphology*, 355, 106677,  
1054 doi:10.1016/j.geomorph.2019.02.021.
- 1055 Glueer, F., S. Loew, A. Manconi, and J. Aaron (2019), From toppling to sliding: progressive evolution  
1056 of the Moosfluh Landslide, Switzerland, *Journal of Geophysical Research: Earth Surface*, n/a(n/a),  
1057 doi:10.1029/2019JF005019.
- 1058 Gor, G. Y., P. Huber, and N. Bernstein (2017), Adsorption-induced deformation of nanoporous  
1059 materials—A review, *Applied Physics Reviews*, 4(1), 011303, doi:10.1063/1.4975001.
- 1060 Grämiger, L. M., J. R. Moore, V. S. Gischig, S. Ivy-Ochs, and S. Loew (2017), Beyond debuttressing:  
1061 Mechanics of paraglacial rock slope damage during repeat glacial cycles, *J Geophys Res-Earth*,  
1062 122(4), 1004-1036, doi:10.1002/2016jf003967.
- 1063 Grämiger, L. M., J. R. Moore, V. S. Gischig, and S. Loew (2018), Thermomechanical Stresses Drive  
1064 Damage of Alpine Valley Rock Walls During Repeat Glacial Cycles, *J Geophys Res-Earth*,  
1065 123(10), 2620-2646, doi:10.1029/2018jf004626.
- 1066 Grämiger, L. M., J. R. Moore, V. S. Gischig, S. Loew, M. Funk, and P. Limpach (2020),  
1067 Hydromechanical rock slope damage during Late Pleistocene and Holocene glacial cycles in an  
1068 Alpine valley, *Journal of Geophysical Research: Earth Surface*, 125(8),  
1069 doi:10.1029/2019JF005494.
- 1070 Gruber, S., L. King, T. Kohl, T. Herz, W. Haeberli, and M. Hoelzle (2004), Interpretation of geothermal  
1071 profiles perturbed by topography: the alpine permafrost boreholes at Stockhorn Plateau,  
1072 Switzerland, *Permafrost Periglac*, 15(4), 349-357, doi:10.1002/ppp.503.
- 1073 Guéguen, Y., and V. Palciauskas (1994), *Introduction to the Physics of Rocks*, Princeton University  
1074 Press.
- 1075 Haberkorn, A., M. Hoelzle, M. Phillips, and R. Kenner (2015), Snow as a driving factor of rock surface  
1076 temperatures in steep rough rock walls, *Cold Reg Sci Technol*, 118, 64-75,  
1077 doi:10.1016/j.coldregions.2015.06.013.

- 1078 Hales, T. C., and J. J. Roering (2007), Climatic controls on frost cracking and implications for the  
1079 evolution of bedrock landscapes, *J Geophys Res-Earth*, 112(F2), doi:10.1029/2006jf000616.
- 1080 Harper, J. T., N. F. Humphrey, W. T. Pfeffer, T. Fudge, and S. O'Neel (2005), Evolution of subglacial  
1081 water pressure along a glacier's length, *Ann Glaciol*, 40, 31-36,  
1082 doi:10.3189/172756405781813573.
- 1083 Holzhauser, H., M. Magny, and H. J. Zumbuhl (2005), Glacier and lake-level variations in west-central  
1084 Europe over the last 3500 years, *Holocene*, 15(6), 789-801, doi:10.1191/0959683605hl853ra.
- 1085 Hugentobler, M., S. Loew, J. Aaron, C. Roques, and N. Oestreicher (2020), Borehole monitoring of  
1086 thermo-hydro-mechanical rock slope processes adjacent to an actively retreating glacier,  
1087 *Geomorphology*, 362, 107190, doi:10.1016/j.geomorph.2020.107190.
- 1088 Kastrup, U., M. L. Zoback, N. Deichmann, K. F. Evans, D. Giardini, and A. J. Michael (2004), Stress  
1089 field variations in the Swiss Alps and the northern Alpine foreland derived from inversion of fault  
1090 plane solutions, *Journal of Geophysical Research: Solid Earth*, 109(B1),  
1091 doi:10.1029/2003JB002550.
- 1092 Keusen, H., and J. Amiguet (1987), Die Neubauten auf dem Jungfrauoch. Geologie,  
1093 Felseigenschaften, Permafrost, *Schweiz. Ing. Archit.*, 30, 31, 17-18.
- 1094 Killick, R., P. Fearnhead, and I. A. Eckley (2012), Optimal Detection of Changepoints With a Linear  
1095 Computational Cost, *Journal of the American Statistical Association*, 107(500), 1590-1598,  
1096 doi:10.1080/01621459.2012.737745.
- 1097 Koo, M.-H., and Y. Song (2008), Estimating apparent thermal diffusivity using temperature time  
1098 series: A comparison of temperature data measured in KMA boreholes and NGMN wells,  
1099 *Geosciences Journal*, 12(3), 255-264, doi:10.1007/s12303-008-0026-5.
- 1100 Krietsch, H., V. S. Gischig, J. Doetsch, K. F. Evans, L. Villiger, M. Jalali, B. Valley, S. Löw, and F.  
1101 Amann (2020), Hydromechanical processes and their influence on the stimulation effected  
1102 volume: observations from a decameter-scale hydraulic stimulation project, *Solid Earth*, 11(5),  
1103 1699-1729, doi:10.5194/se-11-1699-2020.
- 1104 Lappégard, G., J. Kohler, M. Jackson, and J. O. Hagen (2006), Characteristics of subglacial drainage  
1105 systems deduced from load-cell measurements, *J Glaciol*, 52(176), 137-148,  
1106 doi:10.3189/172756506781828908.
- 1107 Lavielle, M. (2005), Using penalized contrasts for the change-point problem, *Signal Processing*,  
1108 85(8), 1501-1510, doi:10.1016/j.sigpro.2005.01.012.
- 1109 Li, Y., K. Leith, M. A. Perras, and S. Loew (2021), Digital image correlation-based analysis of  
1110 hygroscopic expansion in Herrnholz granite, *Int J Rock Mech Min*, 146, 104859,  
1111 doi:10.1016/j.ijrmms.2021.104859.
- 1112 Manconi, A., V. Coviello, M. Galletti, and R. Seifert (2018), Short Communication: Monitoring rockfalls  
1113 with the Raspberry Shake, *Earth Surf. Dynam.*, 6(4), 1219-1227, doi:10.5194/esurf-6-1219-2018.
- 1114 Marmoni, G. M., M. Fiorucci, G. Grechi, and S. Martino (2020), Modelling of thermo-mechanical  
1115 effects in a rock quarry wall induced by near-surface temperature fluctuations, *Int J Rock Mech*  
1116 *Min*, 134, 104440, doi:10.1016/j.ijrmms.2020.104440.
- 1117 McColl, S. T. (2012), Paraglacial rock-slope stability, *Geomorphology*, 153-154, 1-16,  
1118 doi:10.1016/j.geomorph.2012.02.015.
- 1119 McColl, S. T., and D. Draebing (2019), Rock Slope Instability in the Proglacial Zone: State of the Art,  
1120 in *Geomorphology of Proglacial Systems*, edited by T. Heckmann and D. Morche, pp. 119-140,  
1121 Springer International Publishing, Cham.

- 1122 Moore, J. R., V. Gischig, M. Katterbach, and S. Loew (2011), Air circulation in deep fractures and the  
 1123 temperature field of an alpine rock slope, *Earth Surf Proc Land*, 36(15), 1985-1996,  
 1124 doi:10.1002/esp.2217.
- 1125 Morey, W. W., G. Meltz, and W. H. Glenn (1990), Fiber Optic Bragg Grating Sensors, paper presented  
 1126 at Fiber Optic and Laser Sensors VII, SPIE, Boston, United States.
- 1127 Mufundirwa, A., Y. Fujii, N. Kodama, and J. Kodama (2011), Analysis of natural rock slope  
 1128 deformations under temperature variation: A case from a cool temperate region in Japan, *Cold  
 1129 Reg Sci Technol*, 65(3), 488-500, doi:10.1016/j.coldregions.2010.11.003.
- 1130 Pollack, H. N. (1993), Climate-Change Inferred from Borehole Temperatures, *Global Planet Change*,  
 1131 7(1-3), 173-179, doi:10.1016/0921-8181(93)90048-S.
- 1132 Pollack, H. N., S. Huang, and P.-Y. Shen (1998), Climate change record in subsurface temperatures:  
 1133 a global perspective, *Science*, 282(5387), 279-281, doi:10.1126/science.282.5387.279.
- 1134 Pollack, H. N., and S. P. Huang (2000), Climate reconstruction from subsurface temperatures, *Annu  
 1135 Rev Earth Pl Sc*, 28, 339-365, doi:10.1146/annurev.earth.28.1.339.
- 1136 Prager, C., C. Zangerl, G. Patzelt, and R. Brandner (2008), Age distribution of fossil landslides in the  
 1137 Tyrol (Austria) and its surrounding areas, *Nat Hazard Earth Sys*, 8(2), 377-407,  
 1138 doi:10.5194/nhess-8-377-2008.
- 1139 Rajeev, P., and J. Kodikara (2016), Estimating apparent thermal diffusivity of soil using field  
 1140 temperature time series, *Geomechanics and Geoengineering*, 11(1), 28-46,  
 1141 doi:10.1080/17486025.2015.1006266.
- 1142 Riva, F., F. Agliardi, D. Amitrano, and B. Crosta Giovanni (2017), Damage-Based Time-Dependent  
 1143 Modeling of Paraglacial to Postglacial Progressive Failure of Large Rock Slopes, *Journal of  
 1144 Geophysical Research: Earth Surface*, 123(1), 124-141, doi:10.1002/2017JF004423.
- 1145 Rutishauser, A., H. Maurer, and A. Bauder (2016), Helicopter-borne ground-penetrating radar  
 1146 investigations on temperate alpine glaciers: A comparison of different systems and their abilities  
 1147 for bedrock mapping, *Geophysics*, 81(1), WA119-WA129, doi:10.1190/geo2015-0144.1.
- 1148 Rybach, L., and M. Pfister (1994), Temperature predictions and predictive temperatures in deep  
 1149 tunnels, *Rock Mech Rock Eng*, 27(2), 77-88, doi:10.1007/BF01020206.
- 1150 Schneider, S., M. Hoelzle, and C. Hauck (2012), Influence of surface and subsurface heterogeneity  
 1151 on observed borehole temperatures at a mountain permafrost site in the Upper Engadine, Swiss  
 1152 Alps, *The Cryosphere*, 6(2), 517-531, doi:10.5194/tc-6-517-2012.
- 1153 Steck, A. (2011), 1269 Aletschgletscher mit Teil von 1249 Finsteraarhorn, *Geolog. Atlas der Schweiz*  
 1154 1:25000.
- 1155 Stock, G. M., S. J. Martel, B. D. Collins, and E. L. Harp (2012), Progressive failure of sheeted rock  
 1156 slopes: the 2009–2010 Rhombus Wall rock falls in Yosemite Valley, California, USA, *Earth Surf  
 1157 Proc Land*, 37(5), 546-561, doi:10.1002/esp.3192.
- 1158 Styles, T. D., J. S. Coggan, and R. J. Pine (2011), Back analysis of the Joss Bay Chalk Cliff Failure  
 1159 using numerical modelling, *Eng Geol*, 120(1), 81-90, doi:10.1016/j.enggeo.2011.04.004.
- 1160 Wegmann, M., and G. H. Gudmundsson (1999), Thermally induced temporal strain variations in rock  
 1161 walls observed at subzero temperatures, *Lect Notes Phys*, 533, 511-518,  
 1162 doi:10.1007/BFb0104208.
- 1163 Wegmann, M., G. H. Gudmundsson, and W. Haeberli (1998), Permafrost changes in rock walls and  
 1164 the retreat of alpine glaciers: A thermal modelling approach, *Permafrost Periglac*, 9(1), 23-33,  
 1165 doi:10.1002/(Sici)1099-1530(199801/03)9:1<23::Aid-Ppp274>3.0.Co;2-Y.
- 1166 Wegmann, M. R. (1998), Frostdynamik in hochalpinen Felswänden. am Beispiel der Region  
 1167 Jungfrauoch-Aletsch, ETH Zürich.

1168 Welch, L. A., and D. M. Allen (2014), Hydraulic conductivity characteristics in mountains and  
1169 implications for conceptualizing bedrock groundwater flow, *Hydrogeol J*, 22(5), 1003-1026,  
1170 doi:10.1007/s10040-014-1121-5.

1171 Zhu, H. H., B. Shi, and C. C. Zhang (2017), FBG-Based Monitoring of Geohazards: Current Status  
1172 and Trends, *Sensors*, 17(3), doi:10.3390/s17030452.

1173